FACTORS AFFECTING ERROR BOUNDS IN THE USE OF HIGH FREQUENCY RADAR FOR THE REMOTE SENSING OF THE OCEAN SURFACE - AN ANALYSIS INCORPORATING PULSED AND FREQUENCY MODULATED CONTINUOUS WAVE SOURCES

MOSES NORGA

Factors Affecting Error Bounds in the Use of High Frequency Radar for the Remote Sensing of the Ocean Surface – An Analysis Incorporating Pulsed and Frequency Modulated Continuous Wave Sources

by

©Norga Moses

A Thesis submitted to the School of Graduate Studies in partial fulfillment of the requirements for the degree of

Master of Engineering

Faculty of Engineering and Applied Science

Memorial University of Newfoundland

March 2013

St. John's Newfoundland

Abstract

In recent years, there has been a variety of research which has addressed the factors affecting the measurement of error bounds when using high frequency (HF) radar for ocean parameter measurements. The study presented here is conducted in order to identify other important factors that should also be considered in establishing meaningful error bounds on any ocean parameter extracted from the received radar signal. Specifically, this research aims at investigating the fluctuations in the Bragg peaks of the HF radar received spectra based on recent cross section models.

The first part of the research work reviews the electric field equations for the backscattered signals when pulsed and frequency modulated continuous wave (FMCW) waveforms are used as transmitting waveforms. The incident radar signal is assumed to be scattered from the ocean surface, which is represented as a zero-mean Gaussian random process. Various operating parameters are selected to simulate the time series electric field for different conditions, and the power spectral densities (PSD) are calculated by the periodogram method. Again, an investigation is carried out to examine the signal to noise relationship in the Doppler spectra when a pulsed radar system has a noise limited reception. The noise is assumed to be external with no attempt to address internal noise features. It is assumed that the noise is an addditive white Gaussian process. To develop the noise contaminated signal, a suitable noise model is incorporated in the time domain of the electric field signal. The Doppler spectra are calculated and examined

for various signal to noise ratios.

The second part of the research work examines the fluctuations in the Bragg peaks of the received Doppler spectra from the ocean surface. An investigation is first carried out for an ideal noiseless radar system. Choosing various operating frequencies, pulse widths (pulse waveform) and frequency bandwidths (FMCW waveform) for the simulations, numerical examinations of the existance of spectral fluctuations and Bragg distributions are conducted. The centroid positions of the Bragg peaks are calculated and compared with theoretical values to reveal the relative difference. To check the significance of the fluctuations, the standard deviations of the centroid positions of the Bragg regions are analyzed and compared to the resolution imposed by the fast Fourier transform (FFT). The results show that the standard deviations vary for various operating parameters of the radar.

Finally, using the noise model introduced in the first part of the analysis, the investigation of the Bragg fluctuations is extended to a noise limted pulsed radar waveform. The standard deviations of the centroid positions are observed for different signal-to-noise ratios, operating frequencies and pulse widths. The significance of the noise level in the Bragg fluctuations is considered at the end of the analysis.

Acknowledgements

The author would like to thank the Faculty of Engineering and Applied Science, Memorial University of Newfoundland, for giving him the opportunity to conduct this research. The author would also like to express his sincerest gratitude to his supervisor, Dr. Eric Gill, for the guidance, encouragement, support and patience which was shown him throughout his graduate studies.

This work was supported by the graduate student support through Natural Sciences and Engineering research Council (NSERC) and Atlantic Innovation Fund grants to Dr. Eric Gill, for which the author is deeply thankful.

Special thanks to colleagues and friends, in particular Al-Abbass Al-Habashneh, for his valuable suggestions and assistance at various stages of the work.

The author is indebted to his parents and sisters for always encouraging him and standing by his side.

Table of Contents

List of Tables

List of Figures

Table of Symbols

The page numbers below represent the place of first mention of the quantities.

T : Transmitter antenna (p. 12)

R : Receiver antenna (p. 12)

Δl : Length of a vertical dipole (p. 12)

I_0 : Peak value of current distribution $i(t)$ (p. 12)

ω_0 : Radian frequency of the electric field (p. 12)

τ_0 : Radar transmitting pulse duration (p. 12)

$\Delta\rho_s$: Radial width of the scattering patch (p. 12)

c : Light speed in vacuum (p. 12)

t : Time in seconds (p. 13)

$E(t)$: Time domain received electric field (p. 13)

η_0 : Intrinsic impedance of free space (p. 13)

k_0 : Incident electromagnetic wavenumber (p. 13)

P_t : Peak power of the transmitting source (p. 13)

G_t : Free space antenna gain of the transmitting source (p. 13)

ρ_0 : Distance between the scattering patch and radar components (p. 13)

ρ_1 : Distance from radar transmitter to the scattering patch (p. 13)

ρ_2 : Distance from scattering patch to the radar receiver (p. 13)

$F(\cdot)$: Rough spherical earth attenuation function (p. 13)

$\mathrm{Sa}(x)$: Sinc function, $\mathrm{Sa}(x)\left(\frac{\sin(x)}{x}\right)$ (p. 13)

$\vec{K}_1, \vec{K}_2$: Wave vectors of the ocean wave (p. 13)

ω_1 : Wave frequency of ocean wave, $\omega_1 = \sqrt{g\vec{K}_1}$ (p. 13)

ω_2 : Wave frequency of ocean wave, $\omega_2 = \sqrt{g\vec{K}_2}$ (p. 13)

$\vec{K}$: Ocean wave vector (p. 13)

ω : Wave frequency of ocean wave, $\omega = \sqrt{g\vec{K}}$ (p. 13)

$P_{\vec{K},\omega}$: Random Fourier coefficient of the surface (p. 13)

Γ_H : Hydrodynamic coupling coefficient, (p. 14)

Γ_E : Electromagnetic coupling coefficient, (p. 14)

Γ_T : Total coupling coeffcient, $\Gamma_T = \Gamma_H + \Gamma_E$ (p. 14)

g : Acceleration due to gravity ($= 9.8$ m/s^2) (p. 14)

Δ : Normalized surface impedance of the interface (p. 14)

$S_1(\vec{K})$: Directional ocean surface wave spectrum (p. 15)

$g(\theta_{\vec{K}})$: Directional characteristic of the ocean surface (p. 15)

S_{PM} : Pierson-Moskowitz non-directional spectrum (p. 15)

α_{PM} : An empirical constant of Pierson-Moskowitz spectrum, $\alpha = 0.0081$ (p. 15)

U : Wind speed measured at 19.5 m above the ocean surface (p. 15)

$s(K)$: Spread function for ocean wave directional characteristics (p. 15)

$\bar{\theta}(K)$: Dominant wave direction (p. 15)

θ_ω : Wind direction (p. 15)

$P(\omega_d)$: Power spectral density (p. 18)

ω_d : Radar Doppler frequency (p. 18)

Δt : Time interval of periodogram (p. 18)

$\sigma_1(\omega_d)$: First-order radar cross section (p. 18)

A_p : Area of scattering patch (p. 18)

λ_0 : Radar transmitting wavelength (p. 18)

θ_N : Radar look direction (p. 20)

$\sigma_{2P}(\omega_d)$: Second-order radar cross section for a pulse radar system (p. 20)

$\delta(\cdot)$: Dirac delta function (p. 20)

ω_B : Doppler radian frequency of the Bragg peaks (p. 20)

$\epsilon(\cdot)$: Random phase uniformly distributed between 0 to 2 π for every x (p. 23)

δ_k : Kronecker delta function (p. 23)

f_0 : Radar operating frequency (p. 29)

α : Frequency sweep rate (p. 29)

T_r : Frequency sweep interval (p. 29)

ρ_r : Radar range variable for an FMCW waveform (p. 31)

$\Delta\rho$: Range resolution for an FMCW (p. 31)

k_r : $\dfrac{4\pi\alpha\rho_r}{c^2}$ (p. 31)

B : Frequency sweep Bandwidth (p. 31)

k_B : $\dfrac{2\pi B}{c}$ (p. 31)

$Si(x)$: $\displaystyle\int_0^x \frac{\sin(t)}{t}dt$ (p. 31)

Δ_r : Parameter used to define the interaction of bins (p. 31)

Γ_P : Total coupling coefficient for FMCW waveform, $\Gamma_P = \Gamma_E - \Gamma_H$ (p. 31)

$n(t)$: Ambient noise voltage as a function of time (p. 37)

$S_N(\omega')$: Power spectral density of the ambient noise as a function of radian frequency ω' (p. 37)

$h(x)$: Heaviside function (p. 37)

k : Boltzmann's constant, $k = 1.38 \times 10^{-23}$J/K (p. 38)

T_0 : Reference temperature taken as $T_0 = 290$K (p. 38)

F_{am} : external noise figure (p. 38)

P_s : Average power of the signal (p. 40)

P_n : Average power of the noise (p. 40)

$\mathbb{E}[x]$: Expected value of x (p. 45)

$\mathcal{R}(\tau)$: Autocorrelation function (p. 45)

$\mathcal{R}_{E(t)}(\tau)$: Autocorrelation function of signal $E(t)$ (p. 45)

$\mathcal{R}_{n(t)}(\tau)$: Autocorrelation function of signal $n(t)$ (p. 45)

σ_n^2 : Variance of the noise signal (p. 46)

$\mathcal{F}$: Fourier transform (p. 46)

$P_N(f)_{dB}$: Noise power spectral density expressed in dB (p. 46)

Δ_{FFT} : Fast Fourier transform resolution (p. 52)

V_{FFT} : Ocean surface current speed resolution (p. 55)

Chapter 1

Introduction

1.1 Purpose of Research

Over many years, researchers have used various instruments and techniques to gather information about the ocean. Knowledge of parameters such as directional wave height spectra, surface currents velocity and wind fields are used to describe the state of the ocean. This information is important in areas such as offshore oil development, coastguard applications and fisheries research. One of the parameters which is of great interest to oceanographers is the ocean surface currents. Ocean current measurements are used to determine the movement of the water surface, providing useful information in applications such as water pollutant monitoring, search and rescue operations and navigation. Also, long term monitoring of the surface currents is used in fisheries applications, for example, to monitor fish larvae from the location they originate to where they settle and grow to maturity.

Traditionally, oceanographic information has been acquired using technologies such as current meters, pressure sensors and satellite-based instruments such as altimeters. However, these conventional technologies for ocean parameter measurements are expensive and difficult to deploy. Additionally, apart from drifters

the effect of external noise is not included in the fluctuation analysis. In Chapter 4, the analysis of the Bragg fluctuations is extended to a noise limited pulsed system. The statistical properties are examined for different noise levels, operating frequencies and pulse widths.

Chapter 5 presents a summary of results and conclusions, and suggestions for future work.

Chapter 2

The Doppler Spectrum for a Monostatic Radar Configuration Assuming a Pulsed and an FMCW Source

2.1 Introduction

The electric field equations used in this portion of the research are based upon models developed by Walsh and his colleagues for first- and second-order scatter for a monostatic radar configuration using a pulsed and an FMCW source. In this chapter, we first choose a model for the directional ocean wave spectra. Time series of the electric field are simulated using Pierson's model [37] for a zero-mean Gaussian process as a descriptor of the ocean surface. Then, the Doppler spectra are estimated using the periodogram method.

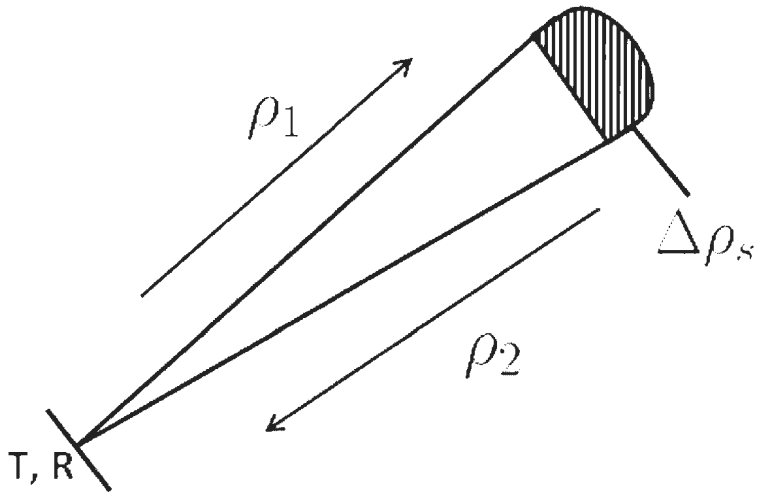

Figure 2.1: Monostatic radar configuration. Symbol meanings are addressed in the text.

2.2 Fourier Series Representation of Electric field Equations for a Pulsed Waveform

For a monostatic radar configuration shown in Figure 2.1 in which the transmitter (T) and receiver (R) are collocated, the analysis leading to the backscattered electric field equations is found in [21] and [38]. Here, the source of the signal is assumed to be a vertical dipole of length Δl with a current distribution of peak value I_0, located at the origin. In this analysis, the current distribution is assumed to be a periodic pulse of radian frequency ω_0 and pulse width τ_0. The scattering patch $\Delta\rho_s$, which is the smallest radial distance that can be unambiguously distinguished by the HF radar, is given by

$$\Delta\rho_s = \frac{c\tau_0}{2} \tag{2.1}$$

where c is the speed of light in vacuum. The Fourier series representation of the electric field equations including the first and second-order scatter as given in [21]

is

$$E(t) = M \sum_{\vec{K},\omega} {}_1P_{\vec{K},\omega} e^{j\omega t} \sqrt{K} e^{j\rho_0 K} \Delta\rho_s \mathrm{Sa}\left[\frac{\Delta\rho_s}{2}(K - 2k_0)\right] + M \sum_{\vec{K}_1,\omega_1} \sum_{\vec{K}_2,\omega_2} {}_1P_{\vec{K}_1,\omega_1} {}_1P_{\vec{K}_2,\omega_2} e^{j(\omega_1+\omega_2)t} \sqrt{K} e^{j\rho_0 K} \Gamma_T \Delta\rho_s \mathrm{Sa}\left[\frac{\Delta\rho_s}{2}(K - 2k_0)\right] \tag{2.2}$$

where M is,

$$\begin{aligned} M &= j\eta_0 k_o^2 I_0 \Delta l \frac{F^2(\rho_0, \omega_0)}{(2\pi\rho_0)^{3/2}} e^{jk_0\Delta\rho_s} e^{-j\pi/4} \\ &= jk_0 \sqrt{8\pi\rho_0 P_t G_t} \frac{F^2(\rho_0, \omega_0)}{(2\pi\rho_0)^{3/2}} e^{jk_0\Delta\rho_s} e^{-j\pi/4} \end{aligned} \tag{2.3}$$

In these equations, η_0 is the intrinsic impedance of free space, k_o is the incident electromagnetic wavenumber, P_t and G_t are the transmitting source peak power and gain respectively, ρ_0 is the distance between the scattering patch and the radar components (i.e., in Fig. 2.1, $\rho_0 = \rho_1 = \rho_2$), $F(\rho_0, \omega_0)$ is the Sommerfeld attenuation function, $\mathrm{Sa}(\cdot)$ is the sampling function $\left(\mathrm{Sa}(\cdot) = \frac{\sin(\cdot)}{(\cdot)}\right)$, $\vec{K}_1$ and $\vec{K}_2$ are first-order ocean wave vectors of radian frequencies ω_1 and ω_2, respectively, Γ_T is the total coupling coefficient as given in equation (2.6) below and t is time in seconds. In equation (2.2), the expression involving the first summation is the contribution of the first-order scatter, that is, a single scatter from a first-order surface wave of wave vector $\vec{K}$ and radian frequency ω. The first-order ocean surface, for which the Fourier coefficients are ${}_1P_{\vec{K},\omega}$, has been verified experimentally to be generally statistically stationary with a normal distribution (see Barrick and Snider [30]) for the typical integration times (on the order of several minutes) used for HF radar ocean measurements. The second-order contribution expression involving the double summation in (2.2) arises as a result of:

- a single scatter from a second-order ocean wave of wave vector $\vec{K}$ which results from the interaction of two first-order ocean waves of wave vectors $\vec{K_1}$ and $\vec{K_2}$ of radian frequencies ω_1 and ω_2, respectivelly; this is referred to as the hydrodynamic second-order scatter.

- a double scatter from two first-order ocean waves of wave vectors $\vec{K_1}$ and $\vec{K_2}$; this is referred to as the electromagnetic second-order scatter. The constraint relating $\vec{K_1}$, $\vec{K_2}$ and $\vec{K}$ appears in Section 2.4.2.

The total coupling coefficient Γ_T associated with these two types of second-order scatter is a combination of the hydrodynamic, Γ_H and the electrodynamic Γ_E [36] and are given by

$$\Gamma_H = \frac{1}{2}\left\{K_1 + K_2 + \frac{g}{\omega_1\omega_2}\left(K_1K_2 - \vec{K_1}\cdot\vec{K_2}\right)\left[\frac{gK + (\omega_1+\omega_2)^2}{gK - (\omega_1+\omega_2)^2}\right]\right\} \tag{2.4}$$

and

$$\Gamma_E = \frac{-|\vec{K_1}\times\vec{K_1}|^2}{2(2k_0)^2\left[\sqrt{-\vec{K_1}\cdot\vec{K_2}} + jk_0\Delta\right]}. \tag{2.5}$$

Hence

$$\Gamma_T = \Gamma_H + \Gamma_E \tag{2.6}$$

where g is the acceleration due to gravity and Δ is the normalized surface impedance of the interface [39].

2.3 Directional Ocean Wave Spectra

To carry out the calculations of the radar cross sections, a particular model needs to be specified for the ocean surface. Here, this model, also used by Gill [40] is discussed in advance.

Several of the ocean spectral models in current use typically consist of a product of a non-directional spectrum $S_1(K)$, and a normalized directional factor, $g(\theta_{\vec{K}})$ where $\bar{\theta}_K$ is the direction of $\vec{K}$(eg. see Kinsman [41] and Tucker [42]):

$$S_1(\vec{K}) = S_1(K)g(\theta_{\vec{K}}) \tag{2.7}$$

with

$$\int_{-\pi}^{\pi} g(\theta_{\vec{K}})d\theta_{\vec{K}} = 1 \tag{2.8}$$

Clearly,

$$\int_0^{2\pi} S_1(\vec{K})d\theta_{\vec{K}} = S_1(K) \tag{2.9}$$

For illustration purposes, the Pierson-Moskowitz non-directional spectrum, S_{PM}, [43] is selected as the ocean wave spectrum with a modification of

$$S_1(K) = \frac{1}{2}S_{PM}(K), \tag{2.10}$$

by Gill [40], where

$$S_{PM} = \frac{\alpha_{PM}}{2K^4}\exp\left(\frac{-0.74g^2}{K^2U^4}\right). \tag{2.11}$$

Here, α_{PM} is a non- dimensional parameter of value 0.0081 and U is the wind speed in m/s measured at 19.5 m above the ocean surface.

In equation (2.7), the directional distribution $g(\theta_{\vec{K}})$, is a function of the wavenumber K, and $\theta_{\vec{K}}$, and taken to be

$$g(\theta_{\vec{K}}, K) = F(s(K))\cos^{2(s(K))}\left[\frac{\theta_{\vec{K}} - \bar{\theta}(K)}{2}\right] \tag{2.12}$$

where $s(K)$ is called the spread function and $\bar{\theta}(K)$ is the dominant direction of the waves [42]. In simulations, it is usual to replace $\bar{\theta}(K)$ by the θ_ω, the wind

direction with respect to the radar look direction. When the frequency dependency is removed from the spread function as is normally done [42], the directional distribution can be written simply as

$$g(\theta_{\vec{K}}) = F(s)\cos^{2s}\left[\frac{\theta_{\vec{K}} - \theta_{\omega}}{2}\right]. \tag{2.13}$$

The normalization in equation (2.7) is satisfied when $F(s)$ is written as

$$F(s) = \frac{2^{(2s-1)}\Gamma^2(s+1)}{\pi\Gamma(2s+1)}, \tag{2.14}$$

where Γ is the gamma function. A typical value of $s = 2$, such has been widely used by previous investigators ([40, 16]), is chosen for our simualtion. For this case

$$F(s=2) = \frac{4}{3\pi} \tag{2.15}$$

The directional ocean wave spectrum may then be written as

$$S_1(m\vec{K}) = \left[\frac{\alpha_P M}{4K^4}\exp\left(\frac{-0.74g^2}{K^2U^4}\right)\right]\left[\frac{4}{3\pi}\cos^4\left(\frac{\theta_{\vec{K}} + \frac{(1-m)\pi}{2} - \theta_{\omega}}{2}\right)\right]. \tag{2.16}$$

In this thesis, all the simulations carried out are based upon this ocean wave model. Figure 2.2 illustrates Pierson-Moskowitz ocean wave spectra for wind speeds of 10 m/s, 12 m/s and 15 m/s. It is obvious that when the wind speed increases, the peak increases in amplitude and shifts towards the lower frequencies. This influences the second-order continuum in the Doppler spectrum causing this continuum to increase in energy and to approach the first order. However, the first-order cross section is not affected to any great extent by the changing wind speeds since the ocean waves that produce the first-order peaks are generally in the saturated, high frequency end of the ocean spectrum. For example, for operating frequencies

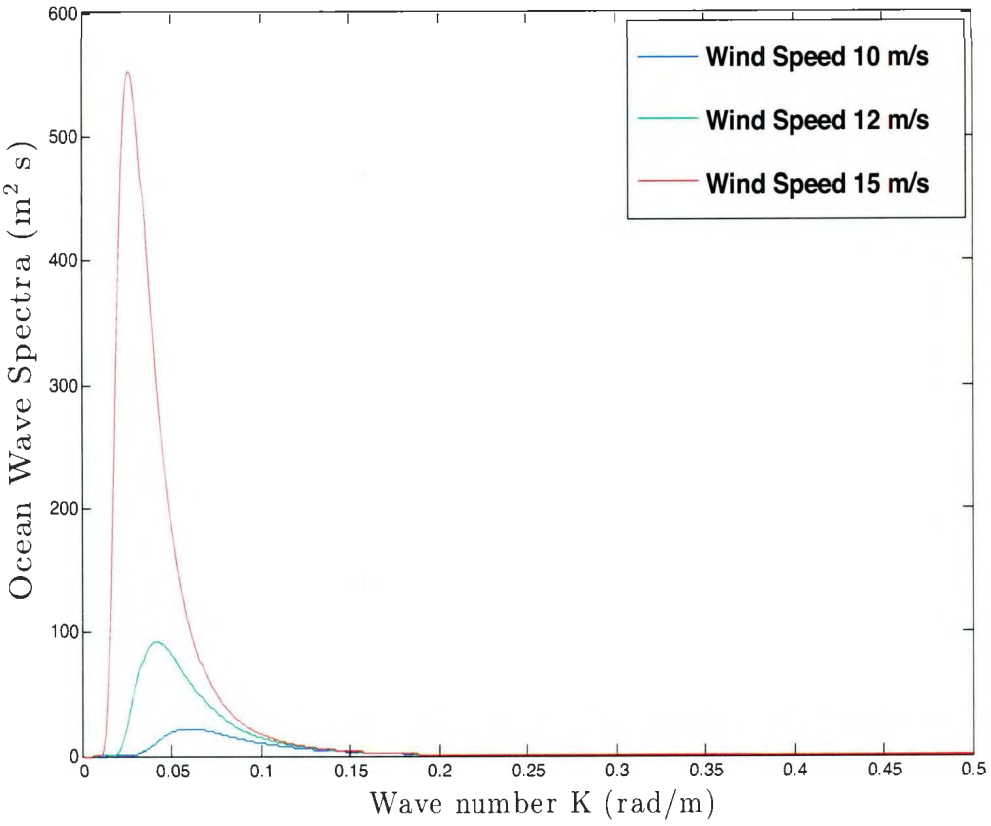

Figure 2.2: Pierson-Moskowitz ocean wave spectrum as a function of wavenumber for different wind speeds.

between 3 to 30 MHz, corresponding to 0.0628 to 0.628, the Bragg peak governed by $2K_0$ occurs for $0.1256 < K < 1.2566$. It may be seen that these values of K are indeed in the high frequency end of S_{PM} and are of nearly constant spectral energy.

2.4 Radar Cross Sections of the Ocean Surface

The radar cross sections for the first- and second-order scatter are obtained by first calculating the power spectral density (PSD) of the time-varying received signal

$E(t)$. The PSD may be obtained by the Fourier transform of the autocorrelation of $E(t)$ [44]. An alternative way of calculating the PSD, as will be used in Section 2.5.1, is the so-called periodogram method, given by [44]

$$P(\omega_d) = \frac{1}{\Delta t}\left|\int_{t_1}^{t_2} E(t)e^{-j\omega t}dt\right|^2 \tag{2.17}$$

where $P(\omega_d)$ is the PSD of $E(t)$ as a function of radian frequency ω_d and the time interval Δt is from t_1 to t_2. The subscript d attached to ω indicates a Doppler radian frequency. From this, the Doppler radar cross section $\sigma(\omega_d)$ may be obtained using the radar range equation given by

$$\frac{P(\omega_d)}{A_p} = \frac{{\lambda_0}^2 P_t G_t G_r |F(\rho_0, \omega_0)|^4}{(4\pi)^3 \rho_0^4}\sigma(\omega_d) \tag{2.18}$$

where A_p is the area of the scattering patch and λ_0 is the radar wavelength.

2.4.1 First-Order Cross Section

The expresson for the first order radar cross section $\sigma_1(\omega_d)$ for a pulsed radar, as obtained in [21], is

$$\sigma_1(\omega_d) = 2^4\pi k_0^2 \sum_{m=\pm 1} S_1(m\vec{K})\frac{K^{\frac{5}{2}}}{\sqrt{g}}\Delta\rho_s \mathrm{Sa}^2\left[\frac{\Delta\rho_s}{2}(K - 2k_0)\right] \tag{2.19}$$

where $S_1(m\vec{K})$ is the ocean directional wave spectrum now given by (2.16) and $\vec{K}$ is the scattering wave vector, ω_d is the radian Doppler frequency, k_0 ($= \frac{\omega_0}{c}$ where c is the speed of light in vacuum) is the radar operating wavenumber and $m = \pm 1$ is used to disinguish the positive and negative portions of the Doppler shifts. The Doppler frequencies ω_d are related to the scattering wavenumbers K by

the dispersion relation, given by

$$\omega_d = -m\sqrt{gK}, \tag{2.20}$$

This means that,

$$m = 1 \text{ when } \omega_d < 0 \tag{2.21}$$

and

$$m = -1 \text{ when } \omega_d > 0. \tag{2.22}$$

Figure 2.3 illustrates an example of the first-order cross section obtained directly using equation (2.19) for an operating frequency of 25 MHz, a wind speed of 15 m/s perpendicular to the radar look direction, and a scattering patch width of 1200 m. It may be noted that, the sampling function Sa(·), that produces the first-order peaks, is maximum when its argument is zero. That is, when

$$K = 2k_0. \tag{2.23}$$

2.4.2 Second-order Cross Section

As stated in Section 2.2, the second-order patch scatter consist of two types of scatter, namely the hydrodynamic second-order scatter, and the electromagnetic. In order to generate the second-order for both cases, the constraint on the wave vectors $\vec{K}_1$ and $\vec{K}_2$, shown in Figure 2.4, is [21]

$$\vec{K} = \vec{K}_1 + \vec{K}_2. \tag{2.24}$$

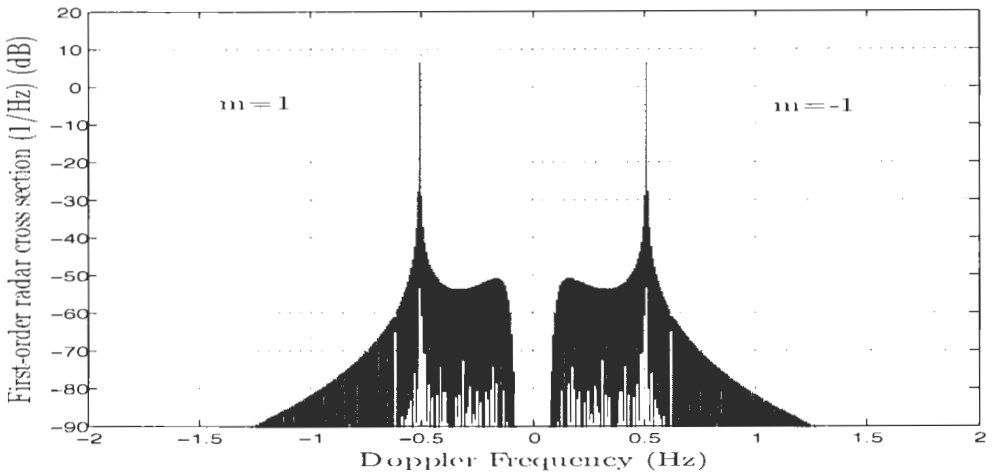

Figure 2.3: An example of the first-order cross section for a radar operating frequency of 25 MHz, wind velocity of 15m/s perpendicular to the radar look direction and a patch width of 1200 m.

where $\vec{K}$ has a magnitude of $2k_0$, in the direction of the radar look direction θ_N. The second order radar cross section for patch scatter as given in [21] is,

$$\sigma_{2p}(\omega_d) = 2^3\pi k_0^2 \Delta\rho_s \sum_{m_1=\pm1} \sum_{m_2=\pm1} \int_0^\infty \int_{-\pi}^{\pi} \int_0^\infty S_1(m_1\vec{K}_1) S_1(m_2\vec{K}_2) |\Gamma_T|^2 K^2 \\ \mathrm{Sa}^2\left[\frac{\Delta\rho_s}{2}(K - 2k_0)\right] \delta(\omega_d + m_1\sqrt{gK_1} + m_2\sqrt{gK_2}) K_1 dK_1 d\theta_{\vec{K}_1} dK \tag{2.25}$$

where $\delta(\cdot)$ is the Dirac Delta function. In equation (2.25) there are four different possible combinations of m_1 and m_2. These combinations represent four distinct portions in the Doppler frequency region of the second-order cross section. For the case of $m_1 = m_2$,

$$\left.\begin{array}{ll} \omega_d < -\omega_B, & \text{when } m_1 = m_2 = 1 \\ \omega_d > \omega_B. & \text{when } m_1 = m_2 = -1 \end{array}\right\} \tag{2.26}$$

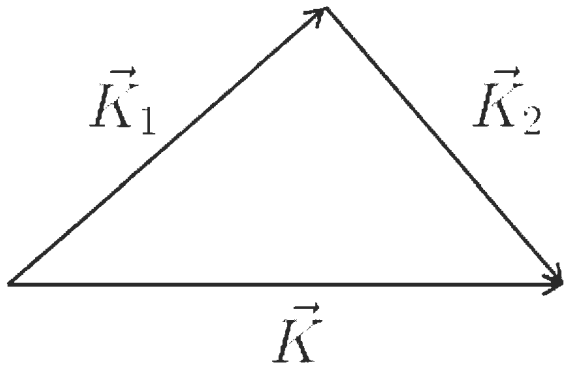

Figure 2.4: Illustration of the second order scatter.

For the case of $m_1 \neq m_2$, $-\omega_B < \omega_d < \omega_B$ and

$$\left.\begin{array}{ll} -\omega_B < \omega_d < 0 & \begin{array}{l} m_1 = -1,\ m_2 = +1 \text{ if } K_1 < K_2 \text{ or} \\ m_1 = +1,\ m_2 = -1 \text{ if } K_1 > K_2 \end{array} \\ \text{and} & \\ 0 < \omega_d < \omega_B & \begin{array}{l} m_1 = -1,\ m_2 = +1 \text{ if } K_1 > K_2 \text{ or} \\ m_1 = +1,\ m_2 = -1 \text{ if } K_1 < K_2 \end{array} \end{array}\right\} \tag{2.27}$$

where ω_B is the Doppler radian frequency of the Bragg peaks. It can be shown that for typical scattering patch widths, the squared sampling function in equation (2.25) may be reduced to a delta function [21]. This simplifies equation (2.25) to

$$\begin{aligned} \sigma_{2P}(\omega_d) \approx & 2^6\pi^2 k_0^4 \sum_{m_1=\pm 1} \sum_{m_2=\pm 1} \int_{-\pi}^{2} \int_{0}^{\infty} S_1(m_1\vec{K}_1) S_1(m_2\vec{K}_2) \\ & |\Gamma_T|^2 \delta(\omega_d + m_1\sqrt{gK_1} + m_2\sqrt{gK_2}) K_1 dK_1 d\theta_{\vec{K}_1} \end{aligned} \tag{2.28}$$

Then, the remaining delta constraint may be solved numerically [17]. An example of the second-order radar cross section is shown in Fig. 2.5 using equation (2.28) for an operating frequency of 25 MHz, a wind speed of 25 m/s, 90^0 to the radar look direction and a scattering patch of 1200 m.

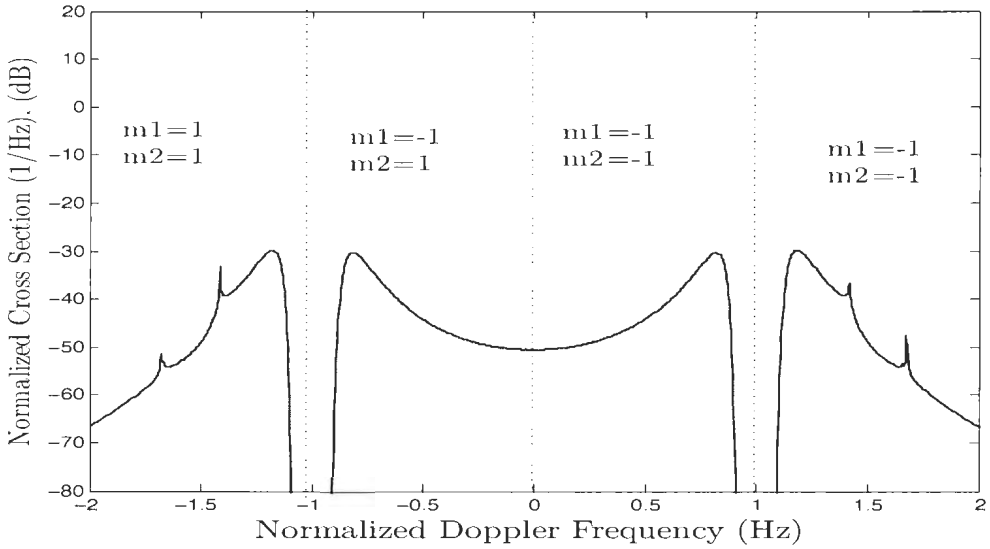

Figure 2.5: The Four portions of the second-order cross section for a radar operating frequency of 25 MHz, a wind velocity of 15 m/s perpendicular to the radar look direction. Only the $K_1 < K_2$ case is simulated here.

Note that in obtaining the cross section expressions and consequently the figures for the first- and second-order scatter (see Figures 2.3 and 2.5) in Sections 2.4.1 and 2.4.2, an infinite time is assumed. Hence, the magnitude and frequency locations of the spectra can be precisely determined. However, in practice, measurement are taken in a finite time. In the next section, a finite time domain series electric field will be simulated and then the Doppler spectra calculated.

2.5 The Simulated Time Series for a Pulsed Source Radar

The electric field equation for a pulsed source radar can be simulated directly using equation (2.2). By considering the $\vec{K}$, ω mesh to be infinitesimal, the sums may

be replaced by integrals. The Fourier coefficients ${}_1P_{\vec{K},\omega}$, of the first order ocean surface may be chosen to have the form [8]

$$ {}_1P_{\vec{K},\omega} = \sum_{m=\pm 1} \sqrt{\frac{1}{2} S(m\vec{K}) d\vec{K}} \delta_k(\omega + m\sqrt{gK}) e^{jm\epsilon(m\vec{K})} \tag{2.29} $$

where δ_k is the Kronecker delta and $\epsilon(m\vec{K})$ is a random phase uniformly distributed between 0 and 2π for each $\vec{K}$. This form for the ${}_1P_{\vec{K},\omega}$ is identical to Pierson's model for a zero-mean Gaussian surface [37]. Substituting equation (2.29) into equation (2.2) and solving the delta function constraint, the backscattered electric field equation for a narrow beam receive array may be written as

$$ \begin{aligned} E(t) = M\sqrt{\Delta\rho_s d\phi} e^{j2k_0\rho_0} \Bigg\{ & \int_K \sqrt{K} e^{j\rho_0(K-2k_0)} \sqrt{\Delta\rho_s} \mathrm{Sa}\left[\frac{\Delta\rho_s}{2}(K-2k_0)\right] \\ & \cdot \sum_{m=\pm 1} \sqrt{\frac{1}{2} S(m\vec{K}) K dK} e^{jm\epsilon(m\vec{K})} e^{-jm\sqrt{gK}t} \\ & + \sqrt{2\pi} k_0 \int_{\vec{K}_1} \sum_{m_1=\pm 1} \sum_{m_2=\pm 1} \sqrt{S(m_1\vec{K}_1) S(m_2\vec{K}_2) d\vec{K}_1}\, \Gamma_T \\ & \cdot e^{jm_1\epsilon(m_1\vec{K}_1)} e^{jm_2\epsilon(m_2\vec{K}_2)} e^{-j(m_1\sqrt{gK_1}+m_2\sqrt{gK_2})t} \Bigg\} \end{aligned} \tag{2.30} $$

In the above equation, $\vec{K}_2 = 2k_0\hat{K} - \vec{K}_1$ and ϕ is the direction of $\vec{K}$. The electric field may be simulated using equation (2.30) by converting the integral equation into a summation equation of the form [37]

$$ \begin{aligned} \psi(t) &= D \int_x e^{j\omega t} e^{j\epsilon(x)} \sqrt{\Xi(x)\frac{dx}{2\pi}} \\ &= D \lim_{\substack{x_{2p}\to\infty \\ (x_{2q+2}-x_{2q})\to 0}} \sum_{q=0}^{p} e^{jx_{2q+1}t} e^{\epsilon(x_{2q+1})} \sqrt{\Xi(x_{2q+1})\frac{x_{2q+2}-x_{2q}}{2\pi}} \end{aligned} \tag{2.31} $$

where D is a constant, p and q are integers and x_0, x_1, $x_2 \cdots$ are net points on the x-axis. Fig. 2.6 shows an example of a 5120-point electric field time series obtained

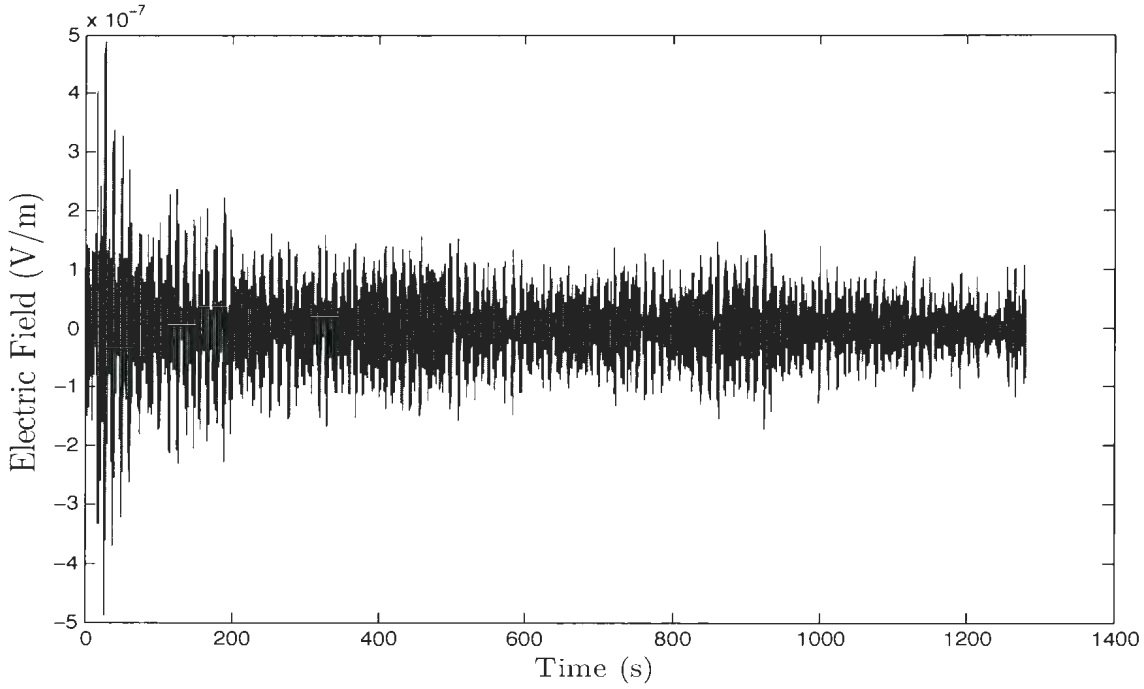

Figure 2.6: An example of a 5120-point simulated first- and second-order scatter times series electric field.

using equation (2.30) when the radar operating frequency is $f_0 = 25$ MHz ($\lambda_0 = 12$ m), $P_t = 16$ kW, $G_t = 2$ dBi ≈ 1.585, $\rho_0 = 50$ km, $\tau_0 = 8$ μs (corresponding to $\Delta\rho_s = 1200$ m), the wind speed is 15 m/s, the wind direction is 90^0 to the radar look direction and a sampling time of 0.25 s are used. The Sommerfeld attenuation function $F(\rho_0, \omega_0)$ is calculated from a Fortran routine developed by Dawe [45]. Figure 2.7, an expanded section of Figure 2.6, shows the existence of sinusoidal components which give rise to the Bragg peaks in the Doppler spectrum (see Figure 2.8)

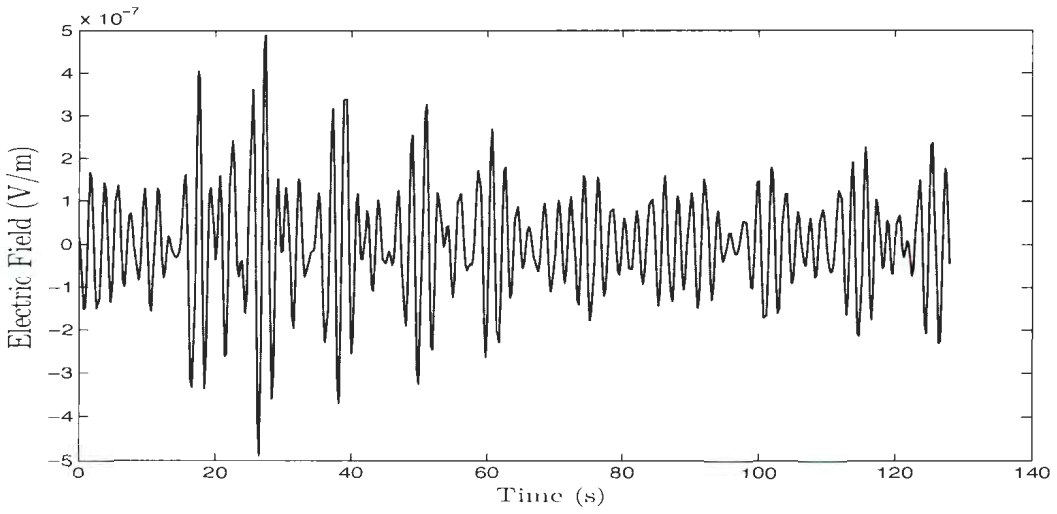

Figure 2.7: An expanded view of Figure 2.6.

2.5.1 The Doppler Spectra

From the simulated time series $E(t)$, the Doppler spectrum can be estimated using the so-called periodogram method given by [44]

$$P(\omega) = \frac{1}{\Delta t}\left|\int_{t_1}^{t^2} E(t)e^{-j\omega t}dt\right|^2 \tag{2.32}$$

where, the time interval is t_1 to t_2, that is $\Delta t = t_2 - t_1$ and $P(\omega)$ is the power spectral density. Another way to calculate the Doppler spectrum is to Fourier transform the autocorrelation [44]. Since the periodogram method is usually used in practice to estimate the Doppler spectrum, it will be employed throughout the analysis. Figure 2.8 shows the power spectral densities estimated as periodograms for different lengths of electric field time series. The parameters used for the simulations are the same as those used for the electric field. In Figure 2.8 (a), the PSD is calculated from a 256-point FFTs, in (b) 512-point FFT and in (c), an average from 10, 512-point FFT with 50% overlap and using a Blackman window.

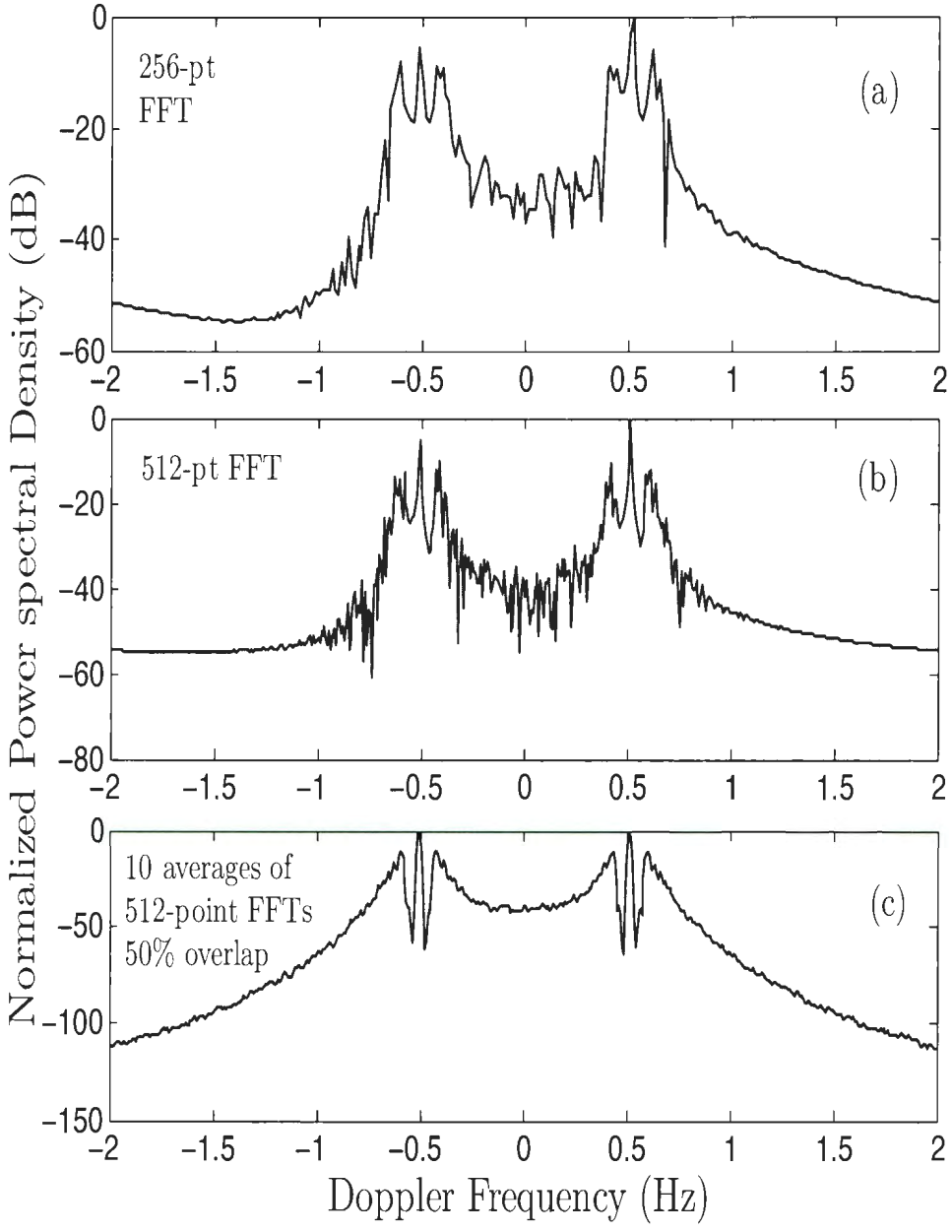

Figure 2.8: A simulated Doppler spectrum for first and second order scatter for a radar operating frequency of 25 MHz and wind direction of 90^0 to the radar look direction. Other parameters are specified in the text.

2.5.1.1 Effects of Wind Direction

The Doppler spectra for wind directions θ_ω of 90^0, 60^0, 30^0 and 0^0 relative to the radar look direction are shown in Figure 2.9. A wind speed of 15 m/s and an operating frequency $f_0 = 25$ MHz are used. It is clearly seen that, the strength of the left and right Bragg peaks differ for different wind directions. When the wind direction is perpendicular to the radar look direction (see Figure 2.9(a)), the energy carried by the two sides is similar, however when the wind direction is 60^0, 30^0 or 0^0 to the radar look direction, one side of the spectrum is greatly enhanced compared to the other (see Figures 2.9(b), 2.9(c) and 2.9(d)). From this property, HF radar can be used to detect wind direction, and studies have been focused in this area by some researchers (for example, see [46],[47],[28])

2.6 Analysis of the FMCW Waveform

2.6.1 Introduction

In the pulse radar system, the width of the pulse determines the range resolution in the system (see equation (2.1)). Clearly, the narrower the pulse, the better the resolution. Then again, the range capabilities of the pulse radar system are determined by the average power in the signal. This means that the peak power in the narrow pulse should be substantial to achieve longer range. Clearly, there is a tradeoff between increasing the range resolution and achieving a longer range. However, the FMCW waveform is known to achieve a higher average power with reasonable peak power. As a result of this, the use of the frequency modulated continuous wave (FMCW) waveform is becoming more and more popular among the HF radar remote sensing community.

In this section, we will develop the time series electric field based on the models

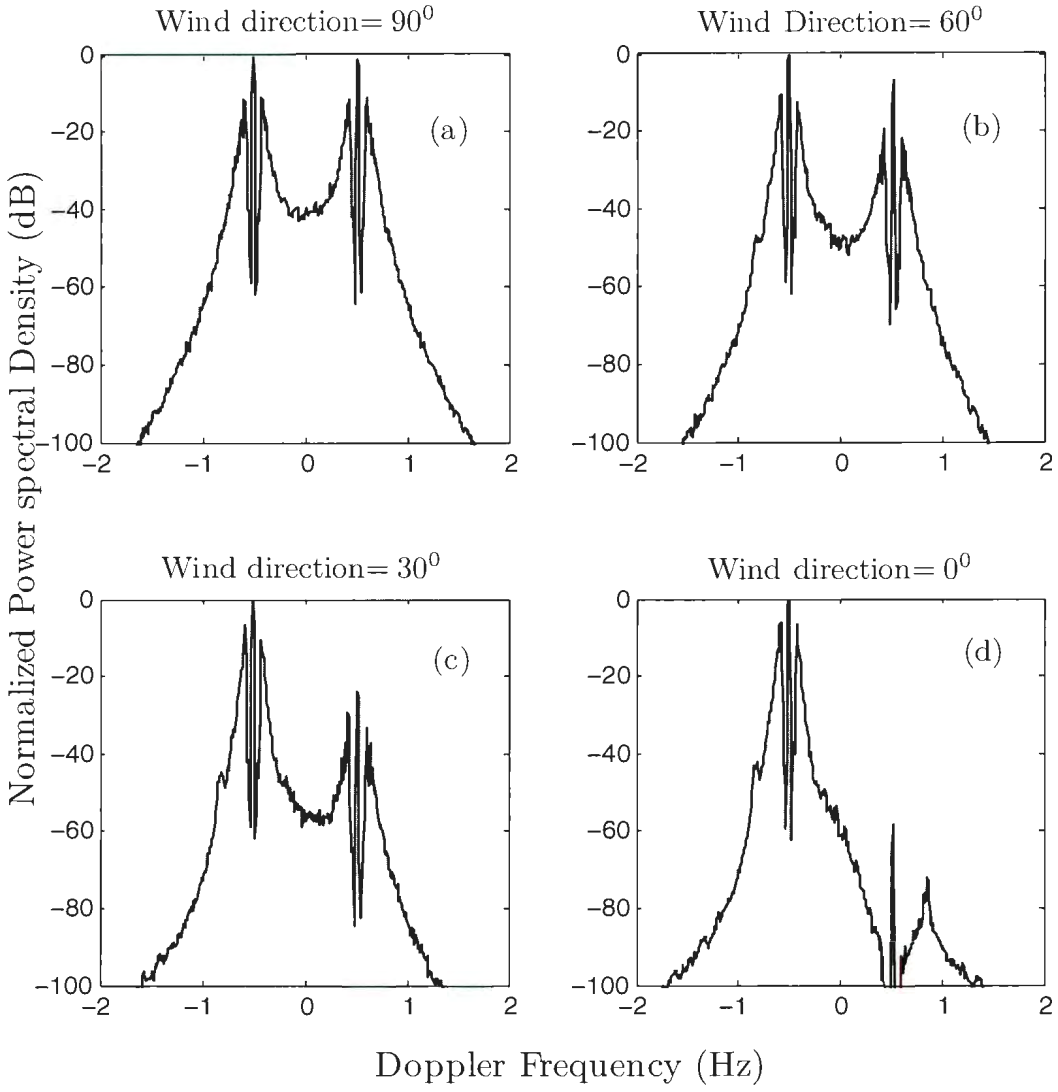

Figure 2.9: Doppler spectrum for a wind speed of 15 m/s with different wind directions of $\theta_\omega = 90^0, 60^0, 30^0$ and 0^0 to the radar look direction. The operating frequency, f_0, is 25 MHz.

derived in [36]. The power spectral densities will be obtained using the periodogram method for different lengths of time.

2.6.2 The FMCW Waveform

In [36], the electric field equations for the backscattered signal are derived by assuming the transmitting dipole to be carrying a frequency-modulated continuous waveform (FMCW) signal $x(t)$ given by

$$x(t) = I_0 \cos\left[2\pi\left(f_0 \pm \frac{\alpha t}{2}\right)\right], \tag{2.33}$$

where I_0 is the peak current, α is the frequency sweep rate, t is time and $\pm$ represents the up and down frequency sweeps and f_0 is the centre frequency of the sweep. As in [36], the up frequency sweep will be considered in this analysis. An example of an FMCW signal and a frequency-time plot is shown in Figure 2.10. The parameters are $I_0 = 1$ A, $f_0 = 40$ Hz, $\alpha = 40$ Hz/s and a sweep time interval $T_r = 1$ s. It can be seen that within a sweep interval $-\frac{T_r}{2} \leq t \leq \frac{T_r}{2}$, the frequency of the signal changes with time from 20 Hz to 60 Hz, with a center frequency of 40 Hz.

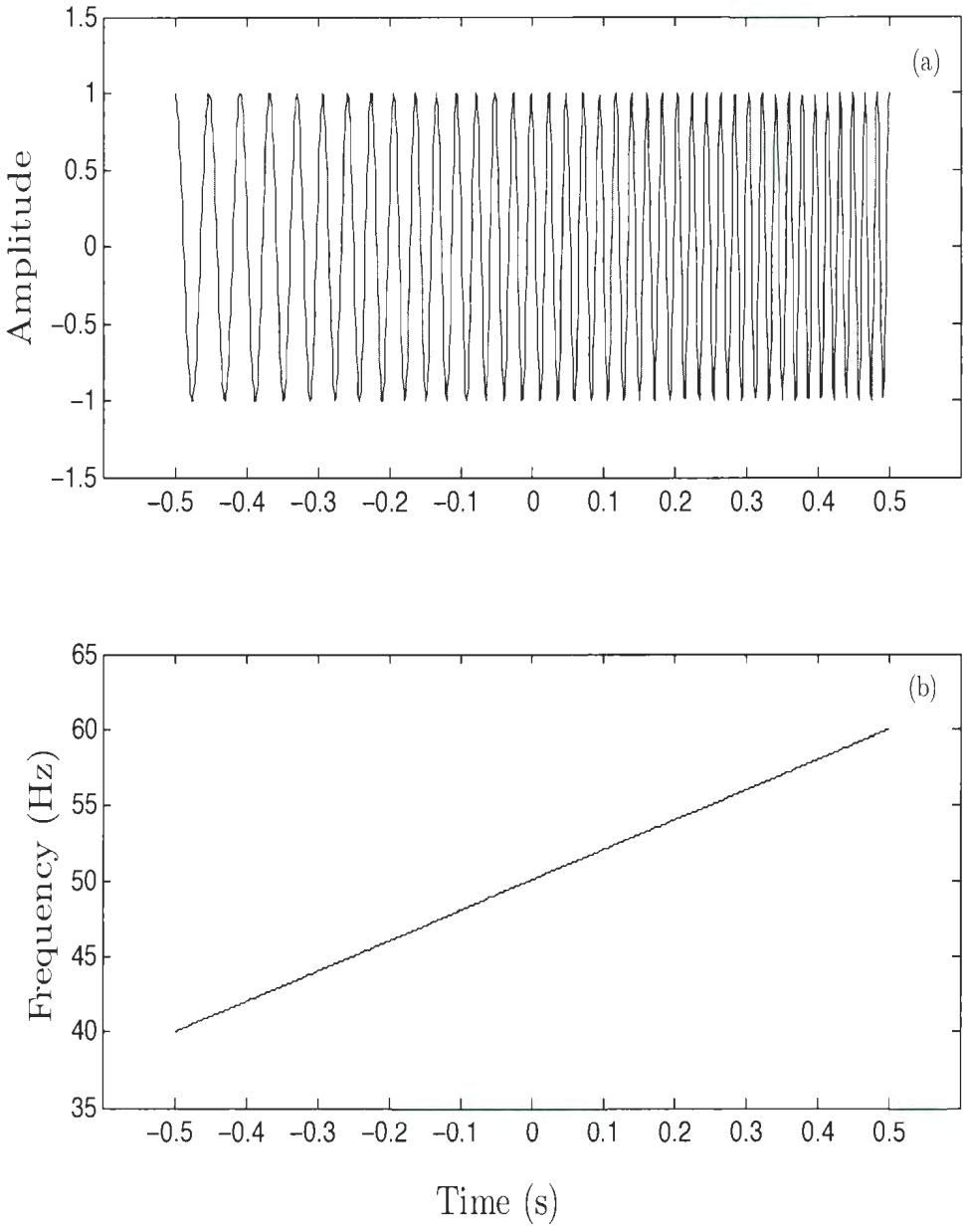

Figure 2.10: An example of the FMCW signal and a frequency-time plot with $f_0 = 40$ Hz and $T_r = 40$ Hz/s.

2.6.3 Electric Field Equations for an FMCW Waveform

As derived in [36], the Fourier series representation of the electric field equations including the first- and second-order for a monostatic radar configuration is

$$E(t) = \frac{jI_0\eta_0\Delta l k_0^2 F^2(\rho_r)}{(2\pi\rho_r)^{3/2}} \left\{ -\sum_{\vec{K},\omega} {}_1P_{\vec{K},\omega}\sqrt{K}e^{-j\pi}e^{j\omega t}e^{j(K-2k_0+k_r)\rho_r}(T_r\Delta\rho)\mathrm{Sm}(K,k_B,\Delta_r) \right.$$
$$\left. + \sum_{\vec{K_1},\omega_1}\sum_{\vec{K_2},\omega_2} {}_1P_{\vec{K_1},\omega_2}{}_1P_{\vec{K_2},\omega_2}\Gamma_P\sqrt{K}e^{-j\pi/4}e^{j\omega t}e^{j(K-2k_0+k_r)\rho_r}(T_r\Delta\rho)\mathrm{Sm}(K,k_B,\Delta_r) \right\} \tag{2.34}$$

In this equation, $F(\rho_r)$ is the Sommerfeld attenuation function, T_r is the sweep time interval, $\Delta\rho$ is the range resolution, ρ_r is the radar range, k_r is a variable defined by

$$k_r = 4\pi\alpha\rho_r/c^2. \tag{2.35}$$

The $\mathrm{Sm}(K,k_B,\Delta_r)$ is defined as

$$\mathrm{Sm}(K,k_B,\Delta_r) = \frac{1}{\pi}\left\{Si[(K-2K_0+k_B)\Delta_r] - Si[(K-2K_0-k_B)\Delta_r]\right\} \tag{2.36}$$

where

$$Si(x) = \int_0^x \frac{\sin t}{t}dt \tag{2.37}$$

In these equations, $k_B = \frac{2\pi B}{c}$(where B is the sweep bandwidth). The parameters $\pm\Delta_r$ appear as integral limits in the analysis leading to the derivation of equation (2.34) [36]. This parameter is used to study the interaction between range bins. Γ_P is the total coupling coefficient associated with the two types of second-order scatter, analogous to Γ_T in equation (2.2) except, as derived in [36],

$$\Gamma_P = \Gamma_E - \Gamma_H \tag{2.38}$$

All other parameters have the same meaning as Section 2.2.

2.6.4 The Simulated Time Series and Doppler Spectrum

Using Pierson's model [37] for a zero-mean Gaussian process, equation (2.34) can be cast as

$$
\begin{aligned}
E(t) = & \frac{jI_0\eta_0\Delta l k_0^2 F^2(\rho_r)}{(2\pi\rho_r)^{3/2}} \Big\{ - \int_{\vec{K}} \sqrt{K} e^{-j\pi} e^{j(K-2k_0+k_r)\rho_r} (T_r\Delta\rho)\mathrm{Sm}(K, k_B, \Delta_r) \\
& \cdot \sum_{m=\pm 1} \sqrt{\frac{1}{2} S(m\vec{K}) d\vec{K}} e^{jm(m\vec{K})} e^{-jm\sqrt{gK}t} \\
& + \int_{\vec{K_1}} \int_{\vec{K_2}} \Gamma_P \sqrt{K} e^{-j\pi/4} e^{j(K-2k_0+k_r)\rho_r} (T_r\Delta\rho)\mathrm{Sm}(K, k_B, \Delta_r) \\
& \cdot \sum_{m_1=\pm 1} \sum_{m_2=\pm 1} \sqrt{\frac{1}{4} S(m_1\vec{K}_1) S(m_2\vec{K}_2) d\vec{K}_1 d\vec{K}_2} \\
& \cdot e^{jm_1\epsilon(m_1\vec{K}_1)} e^{jm_2\epsilon(m_2\vec{K}_2)} e^{-j(m_1\sqrt{gK_1}+m_2\sqrt{gK_2})t} \Big\}
\end{aligned}
\tag{2.39}
$$

where $S(m\vec{K})$ is the directional ocean wave spectrum. The time series electric field may be generated using the same procedure described in Section 2.5 for the pulsed radar waveform. Figure 2.11 shows a 512-point time series for the electric field equation for first- and second order scatter. In this figure, the parameters are $f_0 = 25$ MHz, $B = 500$ kHz, $T_r = 0.5$ s and a wind speed of 15 m/s perpendicular to the radar look direction. All other parameters are the same as Figures 2.6 and 2.7. The power spectral density of the signal is estimated using the periodogram method (see Figure 2.12). The power spectral density (a) of Figure 2.12 is calculated using a 512-point time series and in (b) an average for ten 512-point FFTs are implemented with a 50% overlap. Comparing the Doppler spectra obtained using the FMCW waveform to those of the pulse waveform, it can be observed that the first-order Bragg peaks occur essentially around the same frequency location.

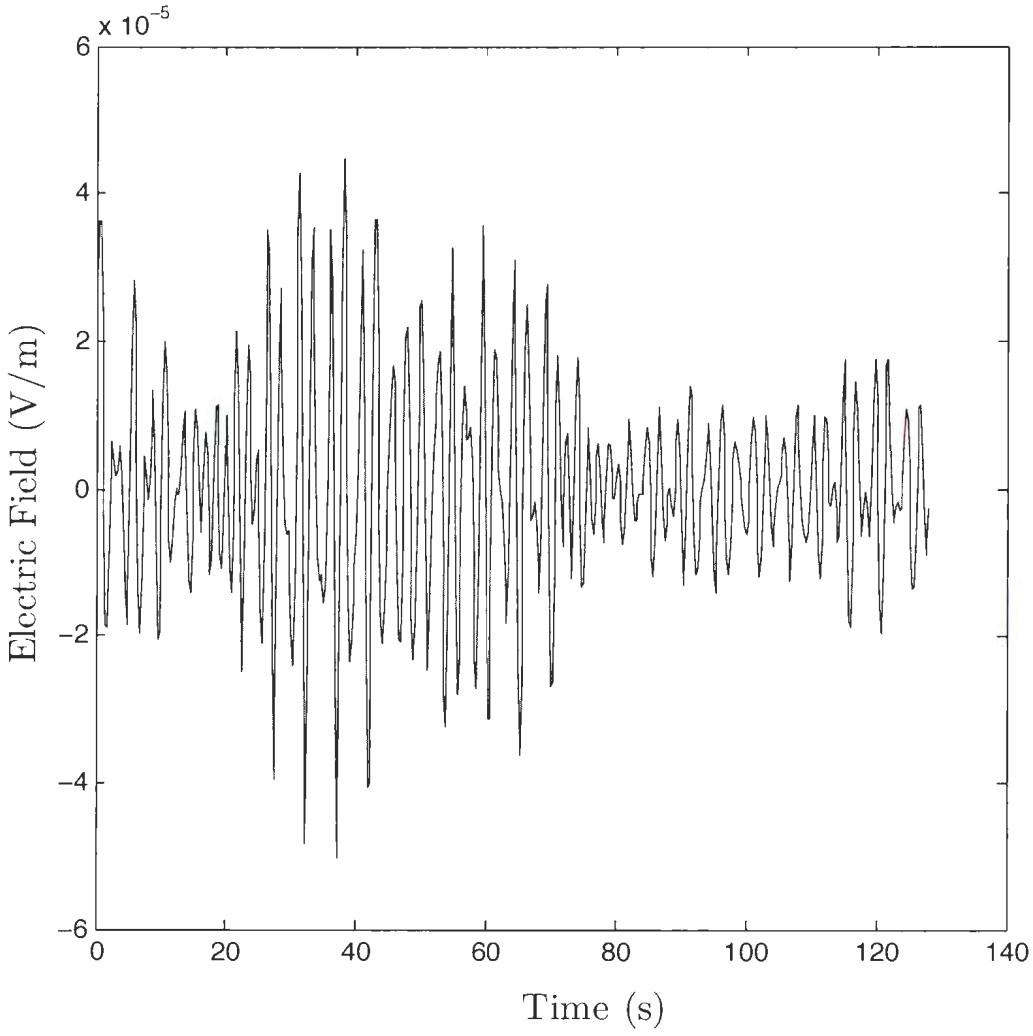

Figure 2.11: An example of a time series electric field for an FMCW waveform with $f_0 = 25$ MHz, $T_r = 0.5$ s and $B = 500$ kHz.

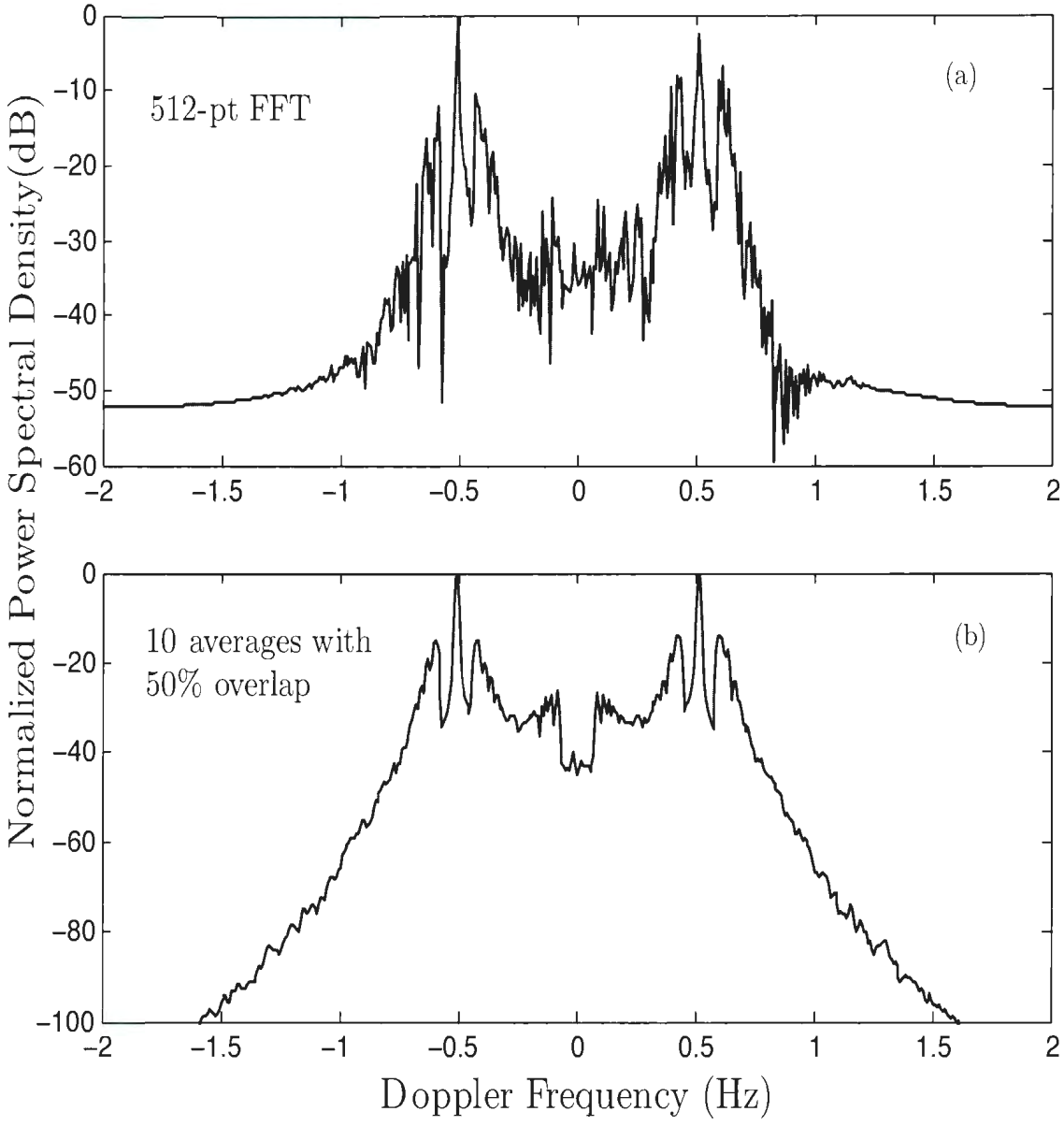

Figure 2.12: Power spectral density calculated from the time series signal for an FMCW waveform. All parameters are as in Figure 2.11.

2.7 General Chapter Summary

The procedure to develop the Doppler spectra from the electric field equations has been reviewed. Beginning from the elctric field equations for a pulsed and an FMCW waveform, the time series are simulated using Pierson's model [37] for a zero-mean Gaussian process as an ocean wave descriptor. The Doppler spectra are calculated using the periodogram. This is demonstrated for various operating parameters and conditions. At this point in the analysis, external noise has not been added to the radar received signal. The random nature of the backscattered signal is due to the randomness of the ocean surface.

Since in practice, the HF radar system has a noise limited reception, there is the need to incorporate a suitable noise model into the backscattered signal. In the following chapter, an external noise model will be defined for the time domain backscattered signal. The signal to noise relationship will be demonstrated for various operating parameters and conditions. This model will be useful in latter analysis in the examination of the fluctuations in Bragg regions of the Doppler spectrum.

Chapter 3

Developing a Suitable Noise Model

3.1 Introduction

Having discussed the Doppler spectrum in Chapter 2, we can clearly see that apart from the scattering surface the strength of the signal received from the ocean depends on various parameters associated with the radar itself. These parameters include the operating frequency of the radar, the gains of the transmitter and receiver antennas, the transmitted power, attenuation functions associated with the medium, the distances of the scattering patch from the radar components and the size of the patch. Since we are using the generally valid assumption that HF radar has an externally noise limited reception, the received signal contains not only useful elements of the ocean clutter but also unwanted noise.

To reflect what generally occurs in practice, this chapter aims at presenting a suitable noise model for a pulsed source HF radar system. In Gill's analysis [40] (also see Gill and Walsh [34]), a suitable model for a zero-mean white Gaussian noise is introduced, and the received clutter signal to noise relationship is

thoroughly examined for a pulsed radar system. In this Chapter, based on Gill's model, the time domain signal of clutter and noise is developed for a pulse radar system. Here, internal system noise will be ignored but could easily be included if the noise figures of the various system components were known. The procedure includes incorporating additive white Gaussian noise into the received electric field equations in the time domain and estimating the power spectral densities using the periodogram method. The effect of noise on the Doppler spectrum will then be examined for different operating parameters and conditions.

3.2 The Time-Domain Noise Model

A model suitable for external noise in the HF radar system is assumed to have the following properties:

- the noise is additive, i.e., the received signal from the ocean surface equals the ocean clutter plus some external noise.
- the noise is white i.e., it has a flat power spectral density. This means, the autocorrelation of the noise signal is zero for any non-zero time offset.
- the noise samples have a normal distribution.

Here, the noise samples are assumed to be statistically independent of the signal. Using Pierson's model [37] for a one-dimensional stationary Gaussian process, the noise voltage $n(t)$ may be written as [34]

$$n(t) = \int_{\omega'} \left[h\left(\omega' + \frac{B}{2}\right) - h\left(\omega' - \frac{B}{2}\right) \right] e^{j\omega' t} e^{j\epsilon(\omega')} \sqrt{S_N(\omega') \frac{d\omega'}{2\pi}}. \qquad (3.1)$$

In the above equation, t is time in seconds, ω' is the radian frequency, $S_N(\omega')$ is the power spectral density of the noise, $\epsilon(\omega')$ is a random phase uniformly distributed

between 0 to 2π for every ω', $h[x]$ is the Heaviside function used to account for the fact that receiver system has a limited noise bandwidth, B. The integral is calculated over the Doppler spectrum band B, where ω' is in the range

$$-\frac{B}{2} \leq \omega' \leq \frac{B}{2} \tag{3.2}$$

The external noise may be man-made or may arise from galactic or atmospheric sources [48]. The nature of the external noise varies with geographic locations, the time of the day and the seasons. Because of these variations, median noise values are used for the simulations.

In equation (3.1) the power spectral density $S_N(\omega')$ is defined as [40]

$$S_N(\omega') = \frac{kT_0}{2\pi} 10^{\frac{F_{am}}{10}} \tag{3.3}$$

where $k = 1.38 \times 10^{-23}$ J/K is the Boltzmann's constant and T_0 is the reference temperature taken as 290 K. F_{am} is an external noise *figure*, available for many geographic regions in documents such as *ITU-R Recommendations* [48]. If the noise figure of a particular operating environment is known, the noise signal may be generated for any bandlimited reveiver system. Figure 3.1 shows the time domain noise signal $n(t)$ for an $F_{am} = 22$ dB and a $B = 500$ kHz. The development of $n(t)$ allows us to simulate the total received signal $E_n(t)$ simply as

$$E_n(t) = n(t) + E(t) \tag{3.4}$$

3.2.1 Signal-to-Noise Ratio (SNR)

The most common and well understood performance measure for the HF radar sytem is the signal-to-noise ratio (SNR). This is normally expressed in decibels

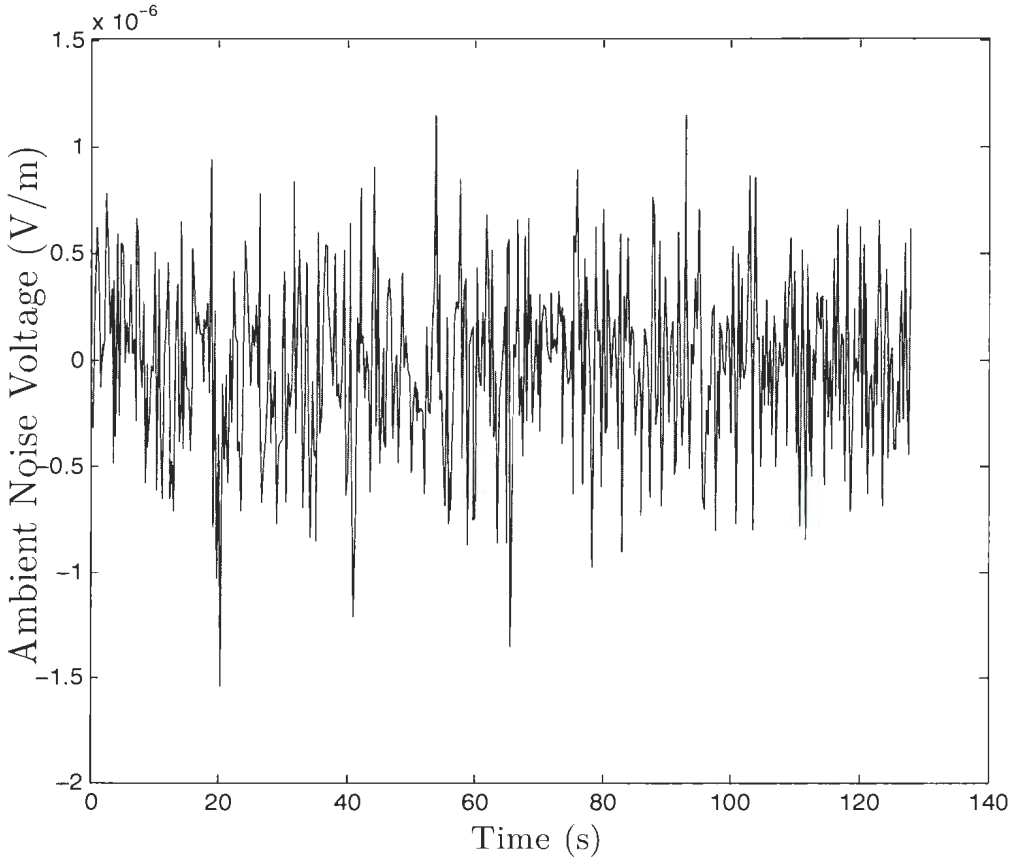

Figure 3.1: The time domain ambient noise voltage for an F_{am} = 22 dB and B = 500 kHz.

(dB). If the average signal power is denoted by P_s and the average noise power, denoted by P_n, the SNR is given by

$$\text{SNR} = \frac{P_s}{P_n} \tag{3.5}$$

The SNR simply measures the strength of the received signal relative to the background noise. In calculating the SNR, the average power of the backscattered signal $E(t)$ may be calculated as [49]

$$P_s = \lim_{t\to\infty} \frac{1}{t} \int_0^t |E(t)|^2 dt \tag{3.6}$$

where t is the observation time in seconds.

3.3 Power Spectral Density

The power spectral density (PSD) of the noise contaminated received signal is depicted in Fig. 3.2. This was obtained using a wind speed of 15 m/s perpendicular to the radar look direction, an operating frequency of 25 MHz, noise figure $F_{am} = 22$ dB and a radar range of 10 km. It is easily observed that the spectral tails of the ocean clutter is buried in the noise floor. If there is an increase in the noise level, significant portions of the ocean spectral density will become buried in the noise floor. This decreases the SNR of the system. Whether or not the SNR increases or decreases depends on various factors such as radar operating frequency, the range at which the measurements were taken and the wind direction. To illustrate the latter point, the behaviour of the PSD will be examined for the cases of different wind directions and different range of measurements for a given noise level:

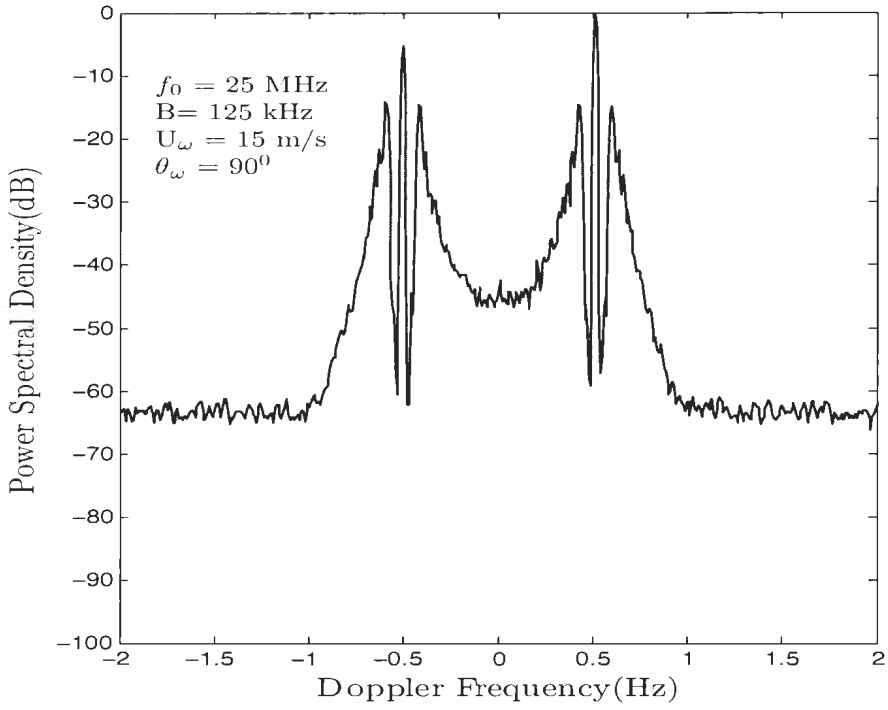

Figure 3.2: An example to illustrate the relationship of the ocean clutter and noise power spectral density for a noise figure of 22 dB

1. **Effects of Wind Directions**

   Fig. 3.3 illustrates the signal to noise relationship for different wind directions of $\theta_\omega = 90^0, 60^0, 30^0$ and 0^0 with respect to the radar look direction. A wind speed of 15 m/s and a radar operating frequency of 25 MHz. The noise figure is kept constant at 22 dB for all the simulation. It can be seen that, when the wind direction is perpendicular to the radar look direction (see Fig. 3.3(a)), the energy carried by the two Bragg peaks is similar, hence the two sides of the doppler spectrum are at the same level above the noise floor. However, when the wind direction is parallel to the radar look direction (see Fig. 3.3(d)), one side of the spectrum will be greatly enhanced above the noise floor whilst the other side is essentially buried in the noise floor. Clearly, whether or not the ocean spectrum exceeds the noise floor depends on the wind direction.

2. **PSD for Different Ranges**

   Fig. 3.4 shows how the signal to noise relationship is affected by different ranges of observations. A wind speed of 15 m/s perpendicular to the radar look direction and an operating frequency of 25 MHz are used. Here, the distances selected are 10 km, 20 km, 30 km and 50 km. The noise *figure* F_{am} = 22 dB is used throughout the simulation. We can see that, not surprisingly, the signal to noise ratio improves significantly at closer ranges. This is due to the fact that, the signal attenuates rapidly with increasing distance.

In practice, it is important to set an acceptable SNR threshold in order to obtain useful measurements from the radar data. All data that falls below the SNR threshold is discarded. If one side of the Doppler spectrum has a higher energy above the noise floor than the other, as is the case of $\theta_\omega = 60^0$ and 30^0 (see Figures 3.3(b) and 3.3(c)), the side with the higher energy is used for ocean parameter

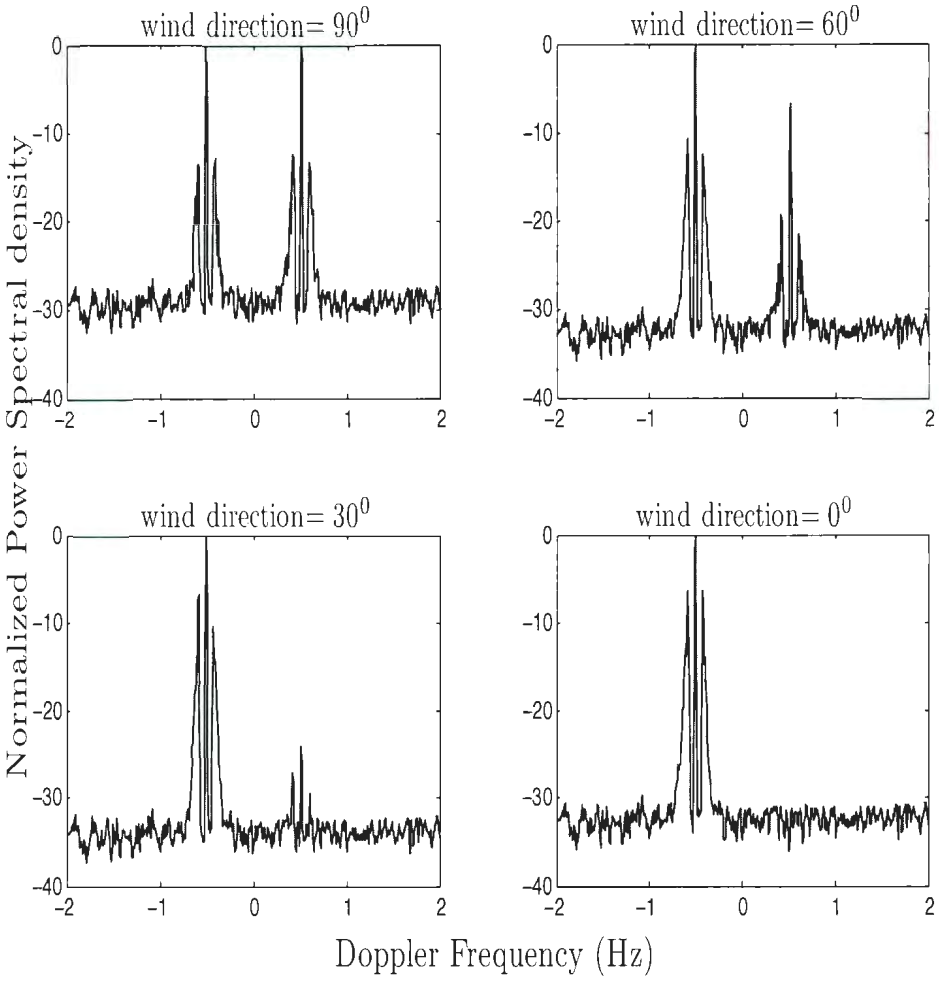

Figure 3.3: The Doppler spectrum for a wind speed of 15 m/s and an SNR of 30 dB for wind directions of $90^0, 60^0, 30^0$ and 0^0 respectively. The radar operating frequency $f_0 = 25$ MHz.

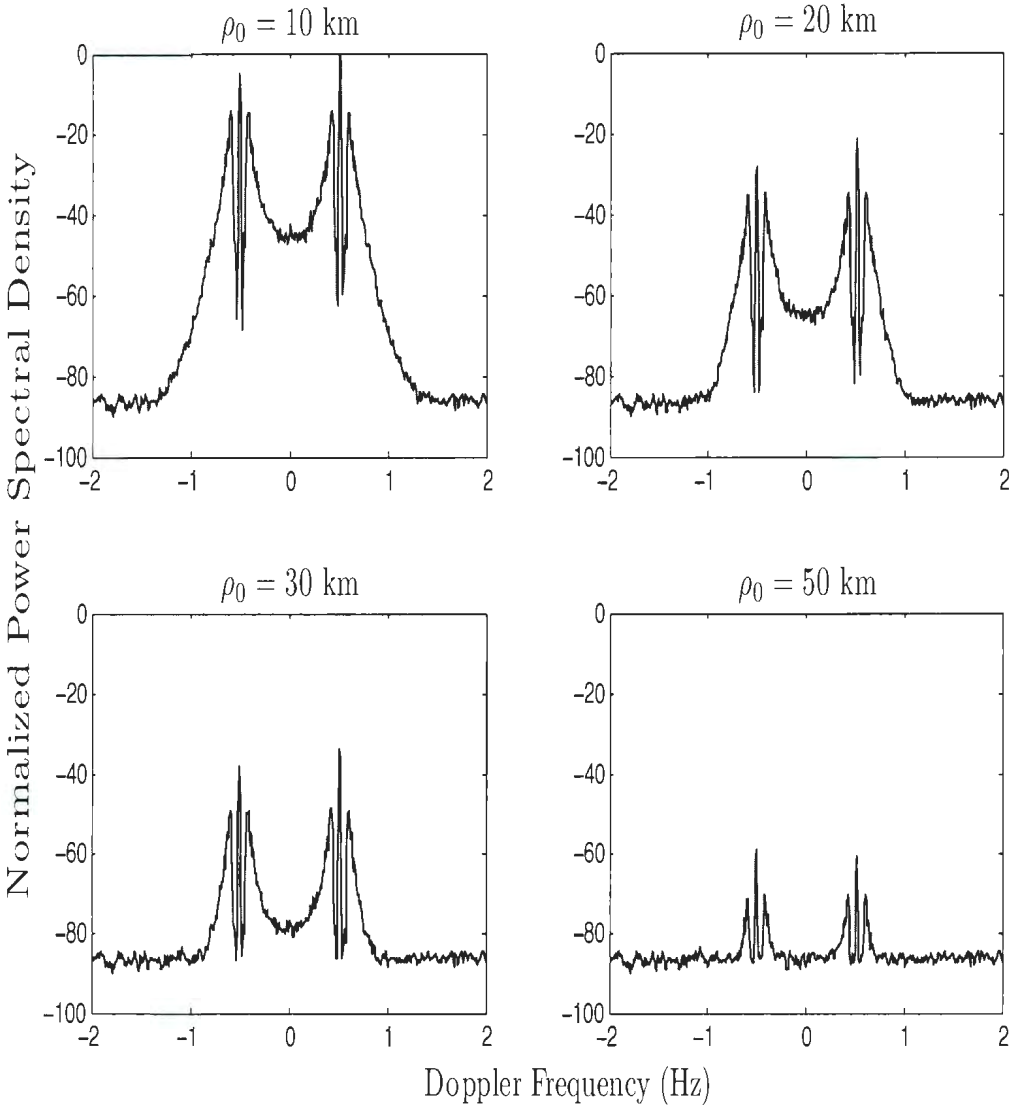

Figure 3.4: The relationship between the ocean and the noise power spectral density for different ranges, ρ_0.

measurements.

3.3.1 Incorporating Noise in the Cross Sections

The noise model may also be incorporated directly into the cross-sections obtained in equations (2.19) and (2.25). As already emphasized, if the received ocean clutter is denoted by $E(t)$, and the external noise is denoted by $n(t)$, the signal received from the ocean is given by

$$E_n(t) = E(t) + n(t) \tag{3.7}$$

where $E_n(t)$ is the received singal. To obtain the power spectral density, the Fourier transform of the autocorrelation of $E_n(t)$ is calculated. The autocorrelation, $\mathcal{R}(\tau)$, of the received signal is given by

$$\begin{aligned}
\mathcal{R}(\tau) &= \mathbb{E}[E_n(t)] && (3.8)\\
&= \mathbb{E}[(E(t) + n(t))(E(t+\tau) + n(t+\tau))] && (3.9)\\
&= \mathbb{E}[E(t)E(t+\tau)] + \mathbb{E}[E(t)n(t+\tau)] + \mathbb{E}[E(t+\tau)n(t)] + && (3.10)\\
&\quad \mathbb{E}[n(t)n(t+\tau)] && (3.11)
\end{aligned}$$

where $\mathbb{E}[x]$ is the expected value of x. If the noise samples are assumed to be statistically independent of the ocean clutter signal, then

$$\mathbb{E}[E(t)n(t+\tau)] = \mathbb{E}[E(t+\tau)n(t)] = 0. \tag{3.12}$$

The autocorrelation reduces to

$$\begin{aligned}
\mathcal{R}(\tau) &= \mathbb{E}[E(t)E(t+\tau)] + \mathbb{E}[n(t)n(t+\tau)] && (3.13)\\
\mathcal{R}(\tau) &= \mathcal{R}_{E(t)}(\tau) + \mathcal{R}_{n(t)}(\tau) && (3.14)
\end{aligned}$$

where $\mathcal{R}_{E(t)}(\tau)$ is the autocorrelation of $E(t)$ and $\mathcal{R}_{n(t)}(\tau)$ is the autocorrelation of $n(t)$. The autocorrelation of $E(t)$ may be found in [21]. Since the bandwidth of the received signal $B \to \infty$, the autocorrelation of the noise signal reduces to

$$\mathcal{R}_{n(t)}(\tau) = \sigma_n^2 \delta(\tau) \tag{3.15}$$

where $\delta(\tau)$ is the delta function and σ_n^2 is the variance of the noise signal. Taking the Fourier transform of $\mathcal{R}(\tau)$ yields PSD of the received signal $\mathcal{P}_{E_n(t)}$ as

$$\mathcal{P}_{E_n(t)}(\omega_d) = \mathcal{F}\{\mathcal{R}(\tau)\} \tag{3.16}$$

However, this assumption is usually an idealisation of physical noise. Since the HF system is a band limited system, the ocean clutter is affected by the noise within this band. In Gill [40], a mathematical expression is obtained to incorporate noise directly into the Doppler spectrum for a bandlimited system. In decibels, the noise power spectral density $P_N(f)$ as a function of frequency f is given by [40]

$$P_N(f)_{dB} = 10\log_{10} P_N(f) = 10\log_{10}(kT_0) + 10\log_{10} 10^{\frac{F_{am}}{10}} = -204 + F_{am} \tag{3.17}$$

3.4 General Chapter Summary

A suitable noise model has been reviewed for a pulsed HF radar system. Based on a noise model introduced by Gill [40] for a pulsed radar waveform, an external noise model is incorporated into the received electric field in the time domain. The Doppler spectra are estimated as periodograms for different operating conditions.

Various wind directions and observation ranges are chosen to investigate the signal to noise relationship. It was shown that the SNR improves greatly or reduces significantly depending on the direction of the wind and the range at which the

measurements are taken.

Having examined the noise model for the received electric field equations, attention will now be focused on applying these results to an examination of appropriate error bounds for ocean surface current measurements in the next chapter.

Chapter 4

Analysis of the Bragg Fluctuations

4.1 Introduction

In surface current measurements, the locations of the Bragg frequencies in the Doppler spectrum of the time-varying electric field voltages described in Sections 2.5 and 2.6.4 are very important. Due to the random nature of the ocean surface, fluctuations occur in the Bragg regions of the Doppler spectra. In order to obtain a better understanding of the errors associated with surface currents measurements, the statistical properties of the Bragg fluctuations were discussed extensively in [8]. However in [8], the effects of external noise on these Bragg fluctuations are not considered in the analysis.

In this chapter, the statistical properties of the fluctuations in the Bragg peaks are first reviewed for an ideal system for both pulsed and an FMCW radar, and then they are examined for the case of an externally noise-limited pulsed radar system. The analysis is conducted for variety of signal-to-noise ratios (SNRs) and radar operating parameters.

4.2 Centroids of the Bragg Peak Region

The measured Bragg frequencies of the Doppler spectrum are taken to be the centroid positions of the Bragg regions. The centroid is defined as the frequency position that divides the Bragg region into two equal areas. The following numerical procedure, presented by Bobby [25], is used to locate the centroids in the Bragg peaks:

1. Locate the positions of the maximum values ω_P and ω_N, in the positive and negative regions of the Doppler spectrum, respectively.

2. Locate the nulls on both sides of the Bragg peaks by calculating the average power over the range of frequencies falling within the intervals known to include the nulls. Here, the intervals chosen are $-1.8\ \omega_N$ to $-1.2\ \omega_N$ and $-0.8\ \omega_N$ to $-0.3\ \omega_N$ for the negative Doppler ranges. The intervals chosen to locate the nulls in the positive Doppler ranges are $1.2\ \omega_P$ to $1.8\ \omega_P$ and $0.3\ \omega_P$ to $0.8\ \omega_P$

3. The nulls are determined as the first set of local values on each side of the peak that fall below the appropriate average.

4. Find the centroid frequency for each side of the Doppler spectrum as that frequency that divides the entire area between the two nulls.

The presence of ocean swell is known to cause a narrow peak between the second- and the first-order Doppler spectrum. This will affect the location of nulls using the algorithm above, but for the purpose of this analysis, the influence of swell will be ignored.

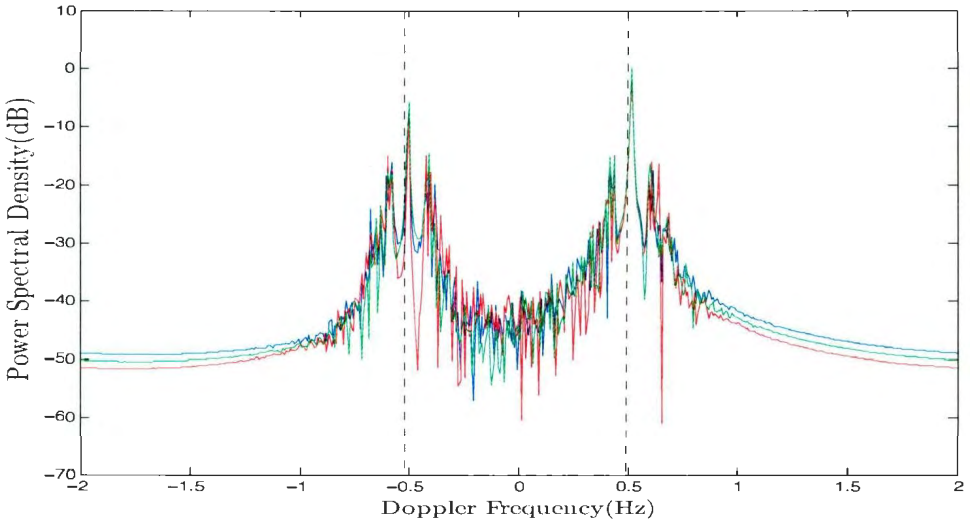

Figure 4.1: Fluctuations of the Bragg region for $f_0 = 25$ MHz and a wind speed of 15 m/s perpendicular to the radar look direction. The centroid positions are indicated as dashed lines from top to bottom.

4.3 Analysis of Bragg fluctuation in a Pulsed Radar Waveform

4.3.1 Introduction

To illustrate the variations in the Bragg peaks, Fig. 4.1 is obtained by segmenting a time series electric field developed using Equation (2.30), into three equal-length consecutive parts, each of length 512 points. The power spectral densities are estimated using the periodogram method and the centroid positions are located for each segment. The centroid positions for each Bragg region are indicated by short dashed lines from top to bottom. A closer look at the left-hand side peak of Fig. 4.1 as presented in Fig. 4.2 shows that the centroid positions of the Bragg region differ for each Doppler spectrum. This indicates that the measured Bragg frequencies for each portion of an extended time series may differ.

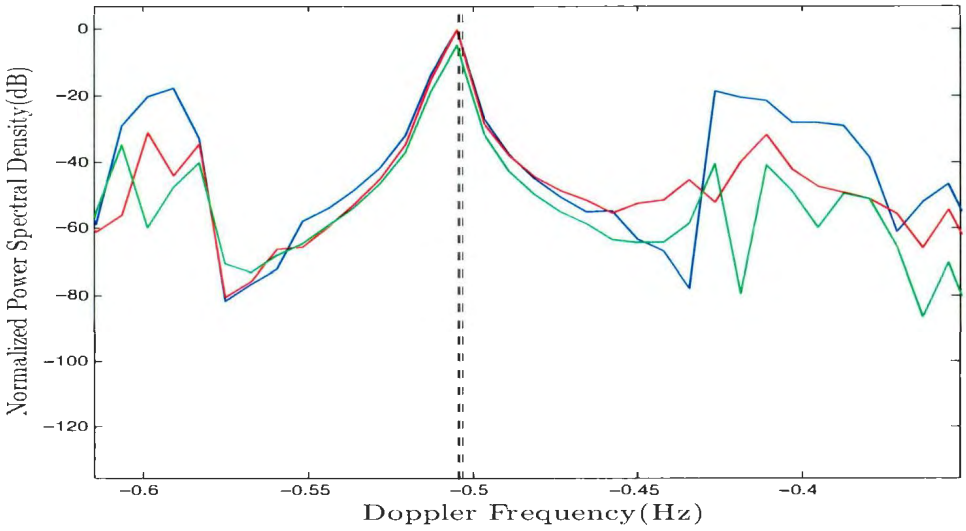

Figure 4.2: A closer look at the left-hand peak of Fig. 4.1.

4.3.2 Distribution of the Bragg Fluctuations

The distribution of the centroid positions has been shown in [8] to depend on the width of the Bragg regions, which in turn, depends on the radar operating parameters such as the frequency, the sampling time and the transmitted pulse width used. In this section, the distribution will be examined numerically for both the positive and negative Bragg regions of the Doppler spectrum.

Throughout the simulations, a constant steady wind velocity of 15 m/s, perpendicular to the radar look direction is used. A time series of 65,536 points (using a sampling rate of 0.25 s, this corresponds to 16384 s), generated using equation (2.30) is segmented into 128 equal-length consecutive parts each containing 512-points. The PSD for each segment is calculated using the periodogram method and centroid positions are determined for a variety of cases as discussed below.

1. **Different Operating Frequencies**:

   Figures 4.3 and 4.4, show the histogram plots of the centroid positions for operating frequencies of 25 MHz and 5 MHz. In calculating the PSD, the dis-

crete Fourier transform (DFT) is implemented using the fast Fourier transform (FFT) algorithm. For each case, a fixed pulse width of 8 μs and a sampling time of 0.25 s are used. An FFT resolution Δ_{FFT} of 0.0078 is imposed by the sampling time. The standard deviations (STD) of the centroid frequencies with respect to the theoretical Bragg frequencies and the FFT resolution Δ_{FFT}, are plotted for comparison. For surface currents measurements, fluctuations are considered to be significant when the standard deviations (STD) exceed 0.5 Δ_{FFT}. It is seen that for an operating frequency of 25 MHz (see Fig. 4.3), the STDs for both the positive and negative Bragg peaks, indicated by the green solid line, are within half the FFT resolution. Thus, the Bragg fluctuations for this case are considered to be insignificant for the given pulse width. However, the Bragg fluctuations are considered significant in the case of a 5 MHz operating frequency (see Fig. 4.4), when the standard deviation exceeds half the FFT resolution. This indicates that the fluctuations vary for different operating frequencies, and in some cases may be significant.

2. **Different Pulse Widths**:

   The distribution of the centroid positions using pulse widths of 7 μs and 2 μs are shown in Figures 4.5 and 4.6, respectively. The same operating frequency of 15 MHz and an FFT resolution of 0.0078 are used for both simulations. The same wind speed of 15 m/s, perpendicular to the radar look direction, is used. When $\tau_0 = 2$ μs (see Fig. 4.6), the measured standard deviations obtained for the left- and right-hand side Bragg peak are 0.0044 and 0.0047 respectively, corresponding to ocean current speed resolutions of 8.8 cm/s and 9.4 cm/s. These exceed half of the Δ_{FFT} of 0.0039, which corresponds to an ocean current speed resolution of 7.8 cm/s. However, when $\tau_0 = 7$ μs,

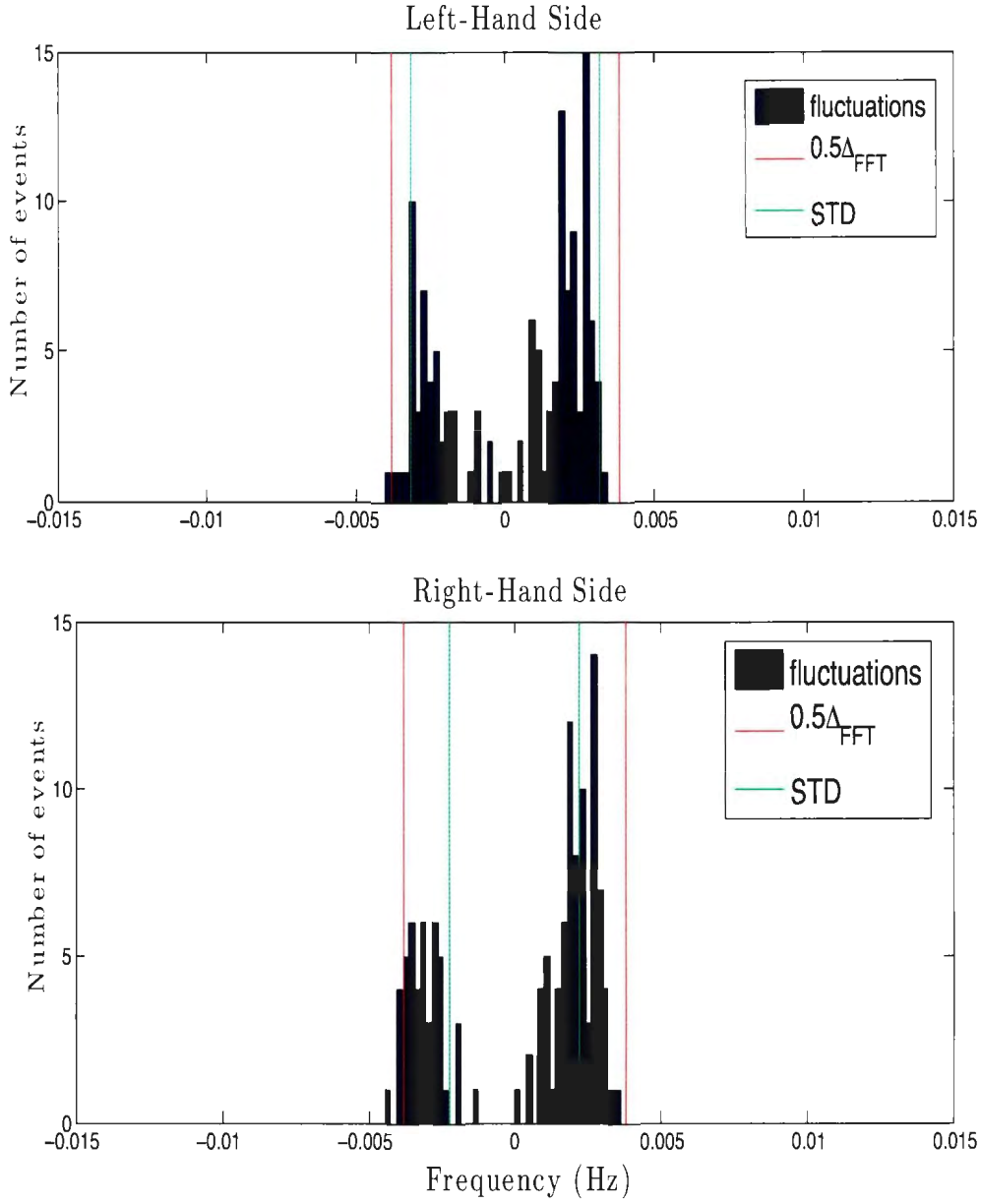

Figure 4.3: The distribution of the centroid positions with f_0=25 MHz and pulse width $\tau_0 = 8$ μs. The abscissa is the frequency difference between the centroid frequency and the theoretical Bragg frequency.

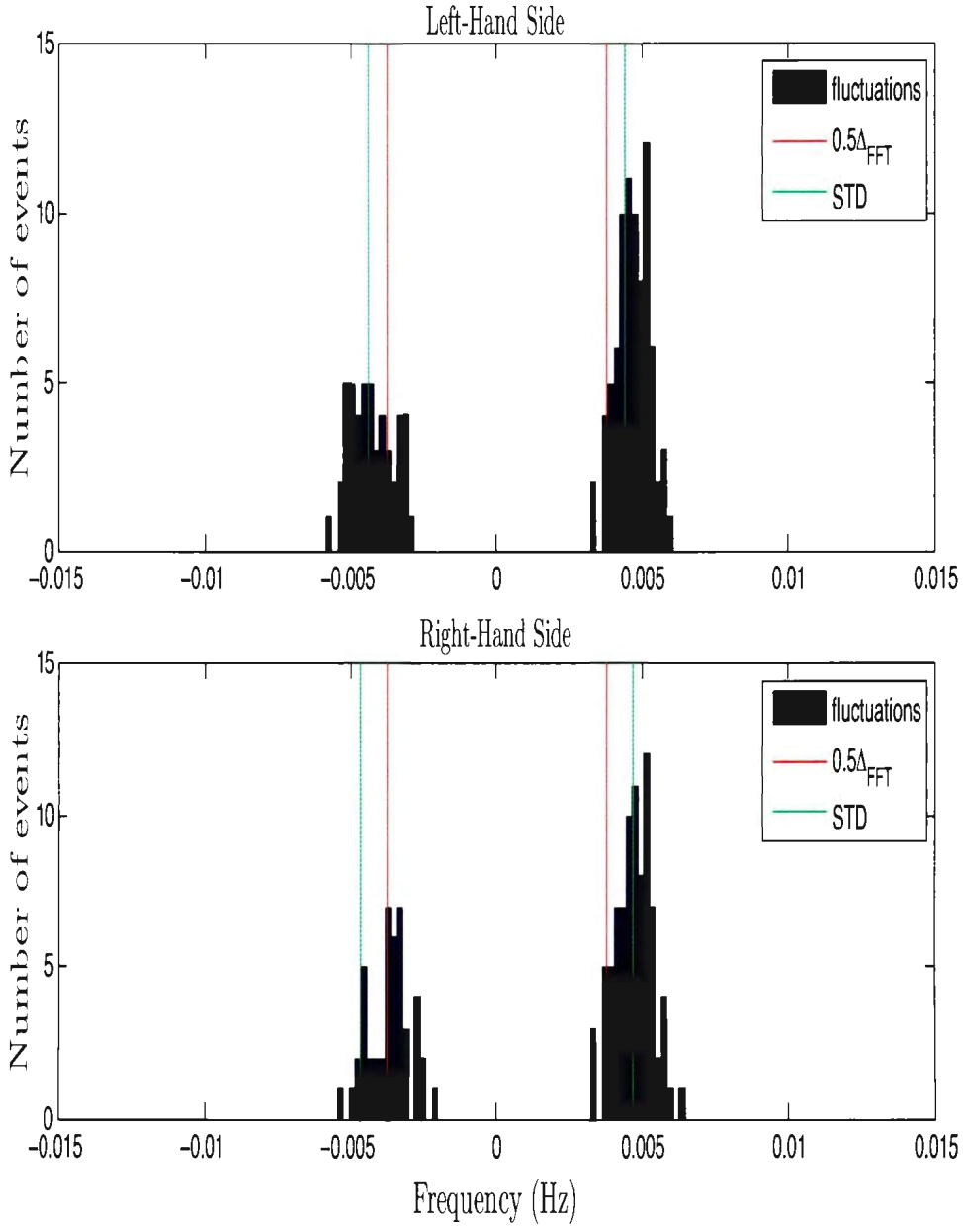

Figure 4.4: The distribution of the centroid positions with f_0=5 MHz and $\tau_0 = 8$ μs.

as seen in Fig. 4.5, the fluctuations are insignificant because the standard deviations of 0.0032 for the left-side peak and 0.0036 for the right-side peak are within the half Δ_{FFT}. These correspond to speeds of 6.4 cm/s and 7.2 cm/s, respectively. Thus, it may be seen that the size of the pulse width may or may not cause significant fluctuations in the Bragg peaks.

To further investigate the dependence of the Bragg fluctuations on pulse widths and operating frequencies, the standard deviations are calculated for other values of these two parameters. Operating frequencies of 25 MHz, 15 MHz and 5 MHz, representing the upper, middle and lower frequency bands are chosen for the simulation. Since the received electric field voltages are stationary Gaussian random variables, the centroids distibutions as well as the calculated standard deviations differ for each realization. As a result, an average standard deviation, calculated from five (5) different realizations is used to estimate the "appropriate" standard deviation using the same operating parameters. Of course a better estimation of the standard deviation will require an average from many more realizations. Figures 4.7 and 4.8 show the plot of the standard deviations of the centroid positions as a function of the pulse width for different operating frequencies. The half Δ_{FFT} are indicated by dashed black lines. The ocean surface current speed resolution V_{FFT}, corresponding to the half Δ_{FFT} will take different values since

$$V_{FFT} = \frac{c\Delta_{FFT}}{2f_0}. \tag{4.1}$$

Tables 4.1, 4.2 and 4.3 provide a summary of the results of Figures 4.7 and 4.8 and their corresponding current speed resolutions. The standard deviations for the left- and right-hand Bragg regions are denoted by STDL and STDR, respectively. V_L and V_R are the calculated ocean current speeds asscociated with the left- and right-hand side standard deviations respectively. Clearly, it can be seen that the standard

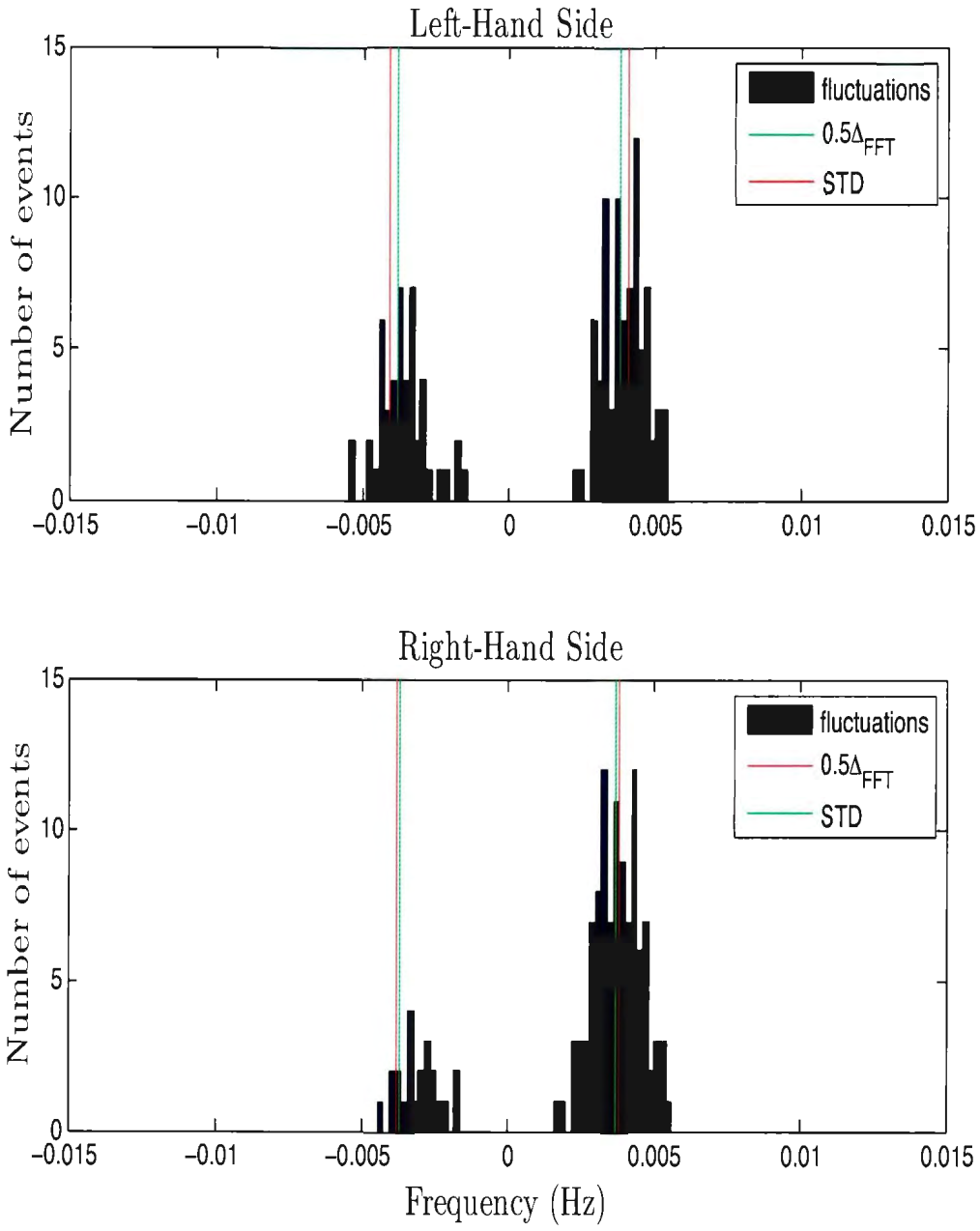

Figure 4.5: The distribution of the centroid positions with f_0=15 MHz and τ_0=7 μs.

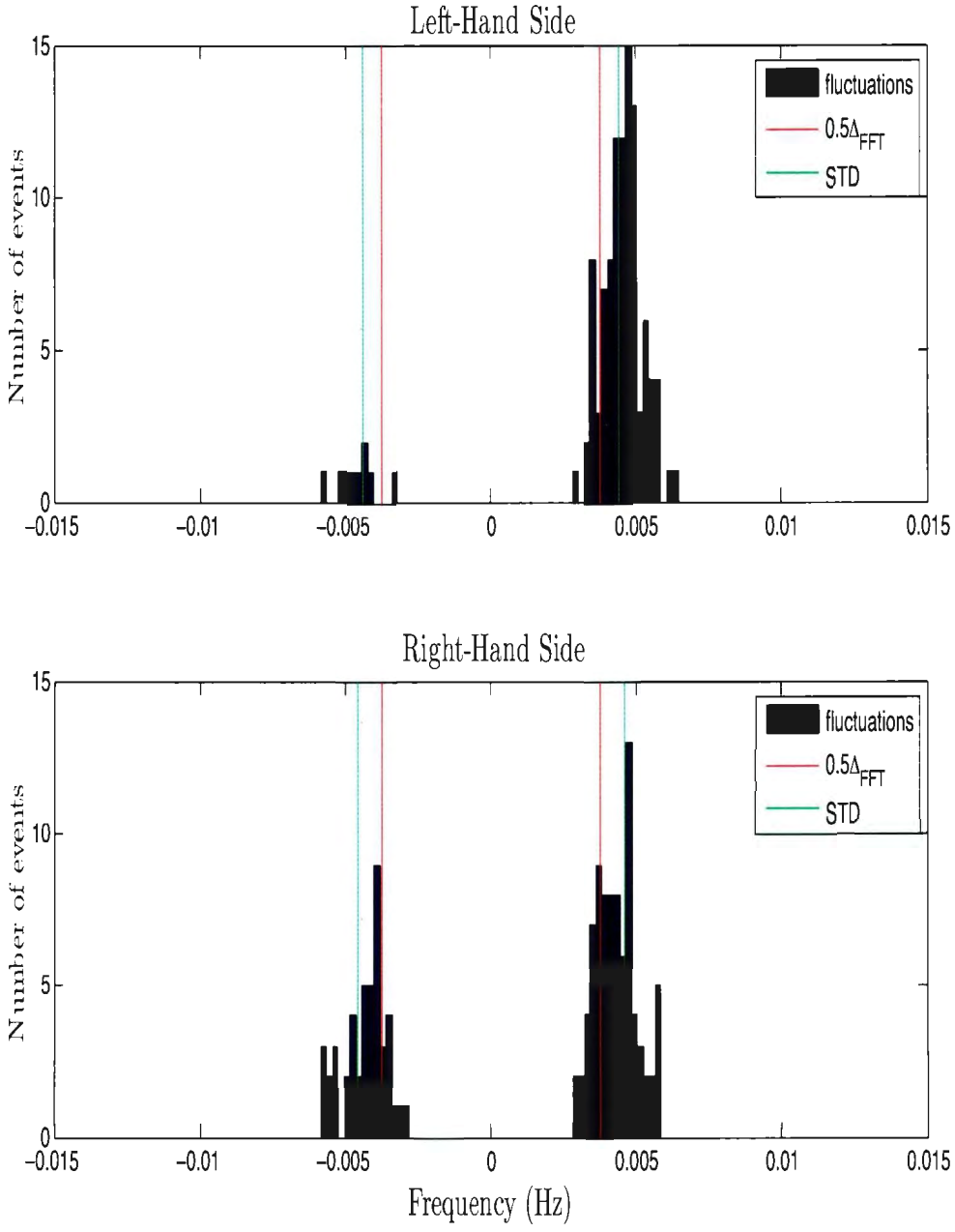

Figure 4.6: The distribution of the centroid positions with f_0=15 MHz and τ_0=2 μs.

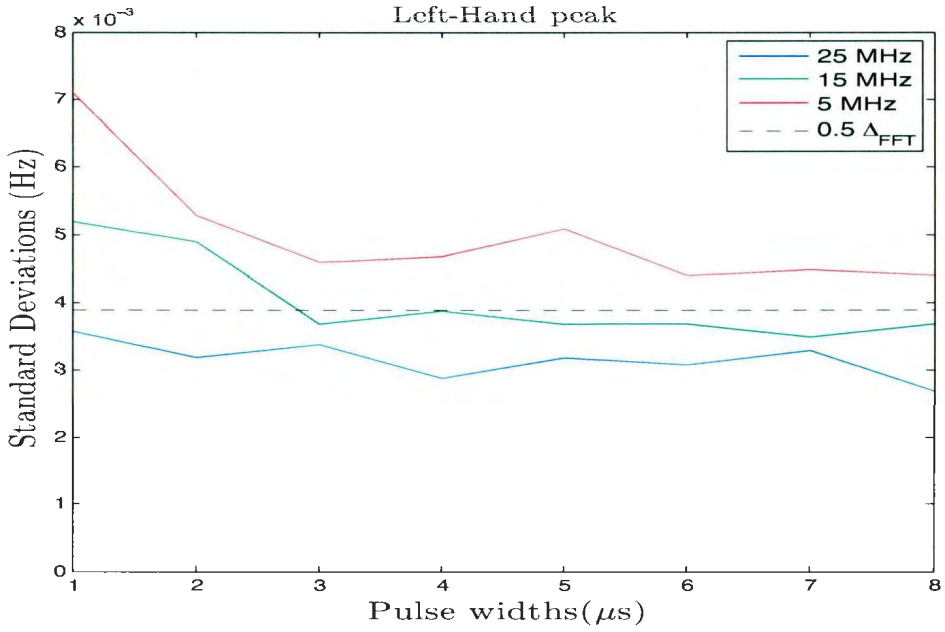

Figure 4.7: Plots of the standard deviations of the centroid positions as a function of the pulse width for different operating frequencies for the left-hand peak.

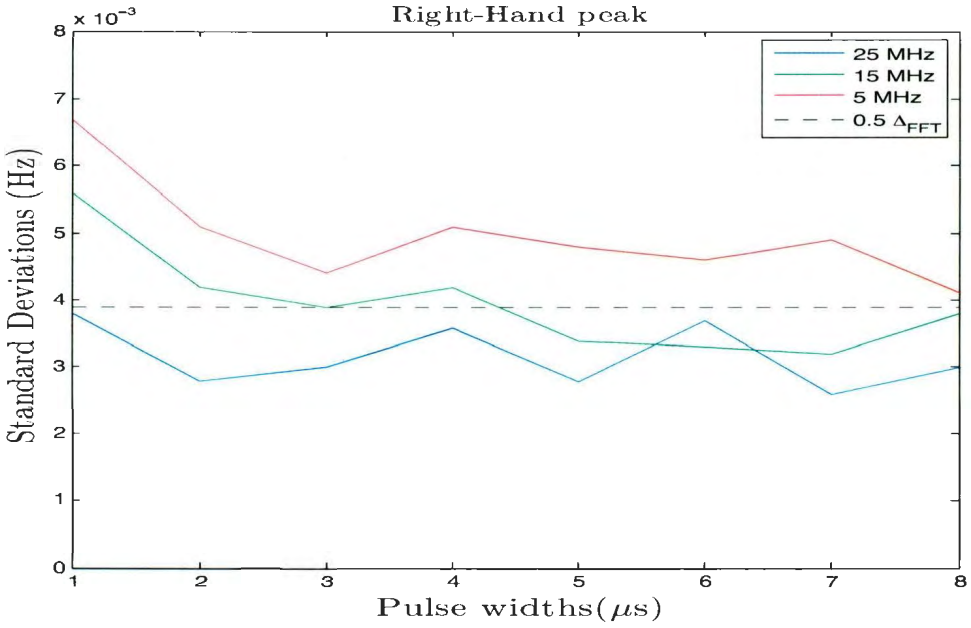

Figure 4.8: Plots of the standard deviations of the centroid positions as a function of the pulse width for different operating frequencies for the right-hand peak.

deviations vary for different operating frequencies and pulse widths. However we notice that the fluctuations are seen to be more significant for lower operating frequencies. For example, we notice that the standard deviations for $f_0 = 15$ MHz and 5 MHz in Figure 4.7 are comparatively more significant than the standard deviations at 25 MHz.

Table 4.1: The STDs for different pulse widths with $f_0 = 25$ MHz. The ocean surface current V_{FFT} associated with $0.5\Delta_{\mathrm{FFT}} = 4.7$ cm/s.

$\tau_0(\mu)$s	STDL (Hz)	V_L (cm/s)	STDR (Hz)	V_R (cm/s)
8	0.0028	3.24	0.0029	3.6
7	0.0033	3.96	0.0026	3.12
6	0.0031	3.72	0.0037	4.44
5	0.0032	3.84	0.0028	3.36
4	0.0029	3.48	0.0036	4.32
3	0.0034	4.08	0.0030	3.6
2	0.0032	3.84	0.0028	3.36
1	0.0036	4.32	0.0038	4.56

Table 4.2: The STDs for different pulse widths with $f_0 = 15$ MHz. The ocean surface current V_{FFT} associated with $0.5\Delta_{\mathrm{FFT}} = 7.8$ cm/s.

τ_0 (μ s)	STDL (Hz)	V_L (cm/s)	STDR (Hz)	V_R (cm/s)
8	0.0037	7.4	0.0038	7.6
7	0.0035	7.0	0.0032	6.4
6	0.0037	7.4	0.0033	6.6
5	0.0037	7.4	0.0034	6.8
4	0.0039	7.8	0.0042	8.4
3	0.0037	7.4	0.0039	7.8
2	0.0049	9.8	0.0042	8.4
1	0.0052	10.4	0.0056	11.2

Up to this point in the analysis, there is no noise or other contamination in the time series. The only source of the fluctuations is due to the randomness of the ocean surface.

Table 4.3: The STDs for different pulse widths with f_0 =5 MHz. The ocean surface current V_{FFT} associated with $0.5\Delta_{\mathrm{FFT}}$ = 23.4 cm/s.

τ_0 (μs)	STDL (Hz)	V_L (cm/s)	STDR (Hz)	V_R (cm/s)
8	0.0044	26.4	0.0041	24.6
7	0.0045	27.0	0.0049	29.4
6	0.0044	26.4	0.0046	27.6
5	0.0051	30.6	0.0048	28.8
4	0.0047	28.2	0.0051	30.6
3	0.0046	27.6	0.0044	26.4
2	0.0053	31.8	0.0051	30.6
1	0.0071	42.6	0.0067	40.2

4.3.3 Standard Deviations for Different Δ_{FFT}

As mentioned earlier in the analysis, the centroid positions of the Bragg peaks are dependent on the width of the Bragg region. For a fixed Δ_{FFT}, the standard deviations of the centroid positions have been shown to be linearly proportional to the width of the Bragg region [8]. However, different Δ_{FFT} will vary the width of the Bragg regions, and this may change the centroid positions of the Bragg peaks. An investigation is carried out to calculate the standard deviations of the centroid position for a different Δ_{FFT}.

In the previous sections, a fixed sampling rate of 0.25 s is used for the simulations. This imposes an FFT resolution $\Delta_{\mathrm{FFT}} = 0.0078$. In this section, a sampling rate of 0.8 s, imposing an $\Delta_{\mathrm{FFT}} = 0.0024$ is used to investigate the significance of the Bragg fluctuations. In Figures 4.9 and 4.10, the standard deviations are plotted against the pulse widths. The parameters used are a wind speed of 15 m/s perpendicular to the radar look direction and operating frequencies of f_0 = 25 MHz, 15 MHz and 5 MHz. Comparing these Figures to Figures 4.7 and 4.8, it can be seen that the standard deviations are relatively higher for a finer FFT resolution. Thus, a sampling rate of 0.8 s as compared to 0.25 s results in relatively

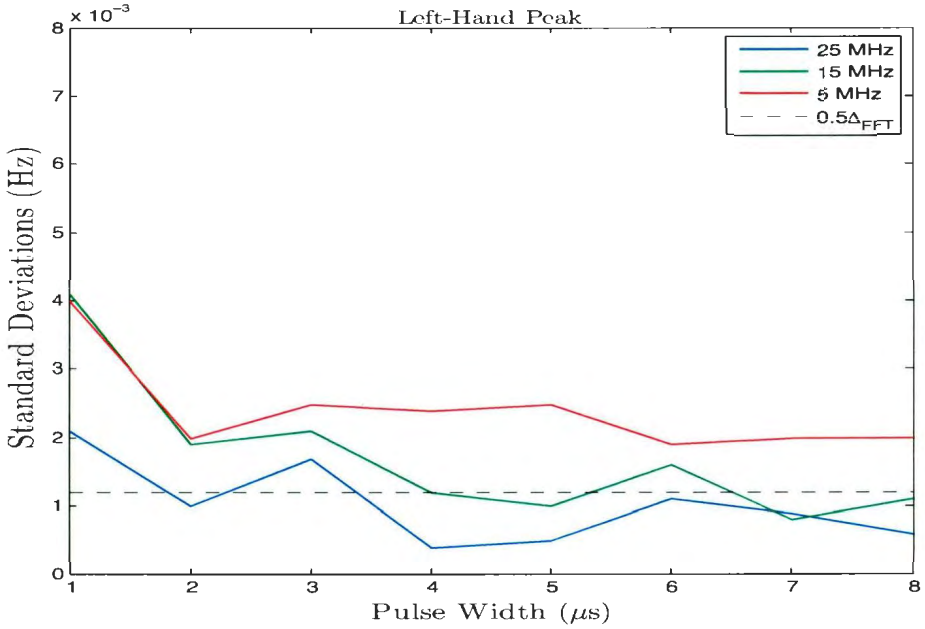

Figure 4.9: The standard deviation of the centroid positions as a function of pulse widths for the left-hand peak using a sampling time of 0.8 s.

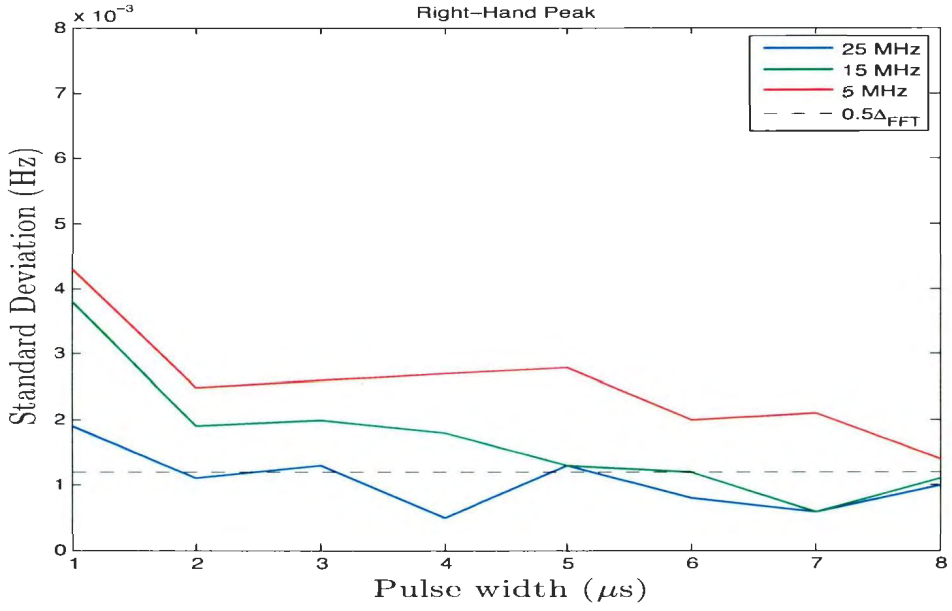

Figure 4.10: The standard deviations of the The standard deviation of the centroid positions as a function of pulse widths for the right-hand peak using a sampling time of 0.8 s.

more significant fluctuations. This is because a finer sampling rate introduces more frequency points to the Bragg region and this adds more randomness in the fixed region. It is also noticed that the Bragg fluctuations are more significant for lower operating frequencies.

4.3.4 Analysis of the Bragg Fluctuations in a Noise Limited Pulsed Radar System

Having investigated the Bragg fluctuations in a noiseless ideal HF radar system, attention will now be focused on investigating the significance of external noise on ocean current measurements. The aim of this analysis is to help in estimating the errors associated with ocean surface current measurements in a typical operating environment.

4.3.5 Doppler Spectra and Centroids of the Bragg Peak Regions

Incoporating the noise model developed in Section 3.2 into the electric field equation and developing the Doppler spectra, the centroid positions of the Bragg regions are estimated numerically using the same algorithm as described in Section 4.2.

4.3.6 Calculation of the Standard Deviation

The standard deviations of the centroid positions with respect to the theoretical Bragg frequencies are calculated for different noise levels. The SNR chosen for this simulation is 30 dB, 20 dB and 10 dB.

Table 4.4 shows how the changing SNR affects the standard deviations of the centroid positions for an operating frequency of 25 MHz and a pulse width of 8 μs.

In this analysis, the same electric field signal is used in combination with different noise levels. Here, the standard deviations estimated for each SNR is an average from five realizations. Half of Δ_{FFT} is 0.0039, corresponding to a ocean current resolution of 4.68 cm/s. All parameters have the same definitions as in Table 4.1.

Table 4.4: The STDs for an operating frequency $f_0 = 25$ MHz, pulse width $\tau_0 = 8$ μs and 0.5 $\Delta_{\mathrm{FFT}} = 0.0039$ Hz corresponding to a speed of 4.68 cm/s.

SNR (dB)	STDL (Hz)	V_L (cm/s)	STDR (Hz)	V_R (cm/s)
∞	0.0028	3.36	0.0026	3.12
30	0.0029	3.48	0.0034	4.08
20	0.0025	3.00	0.0028	3.36
10	0.0036	4.32	0.0039	4.68
0	0.0056	6.72	0.0053	6.24

It is seen that, when the SNR is high, such as ∞ dB, 30 dB or 20 dB, the standard deviations of the centroid positions are barely affected by the noise level making the Bragg fluctuations insignificant. However, as the SNR reduces towards 0 dB, the standard deviations start to go beyond the half Δ_{FFT}, making the fluctuations in the Bragg peaks significant. This is because when the SNR approaches 0 dB, the algorithm used to locate the centroid position becomes less and less accurate. The second order nulls are affected by the noise level and that makes it difficult for the algorithm to accurately locate the nulls. Note that, since an average of five realizations is used to calculate the standard deviations, the results for SNRs of ∞ dB, 30 dB and 20 dB are close enough to be considered the same. Therefore, for these operating parameters, the threshold for the SNR could be considered to be 10 dB for minimal errors.

To explore this further, the analysis is extended to different operating frequencies and pulse widths to check the dependencies of the standard deviations on these parameters when the signal is noisy. Figures 4.11 and 4.12 are plots of the stan-

dard deviations of the centroid positions as a function of the radar pulse width and SNR for an operating frequency of 25 MHz. Similarly, Figures 4.13 and 4.14, are for an operating frequency of 15 MHz. The standard deviations for an operating frequency of 5 MHz are also shown in Figures 4.15 and 4.16. Half the Δ_{FFT}, is indicated by a solid line. We can see from these Figures that when SNR=30 dB or 20 dB, the standard deviations are essentially similar to an ideal noiseless system. This is because, the noise floor in the Doppler spectrum is too low to have any effect on the area covered by the Bragg peaks. Therefore, for these SNRs, the standard deviation of the centroid positions of the Bragg regions are not affected much by the noise. However, when the SNR is 10 dB, the standard deviations are significantly different from that of an ideal noiseless system. This is due to the fact the fluctuations of the noise floor that is closer to the second-order peaks affects the location of the nulls using the algorithm above.

Another conclusion that can be drawn from these figures is that the Bragg fluctuations are seen to be more significant at lower operating frequency band than that at high operating frequency band. However, in general, a high SNR is required to minimize the errors in currents measurements.

4.4 Analysis of the Bragg Fluctuations in an FMCW Waveform

In this section, the Bragg fluctuation analysis is extended to the FMCW waveform, but without the inclusion of noise. The statistical properties are examined for various operating frequencies and bandwidths using the same procedure as in the pulsed waveform. To illustrate the Bragg fluctuations phenomenon, the electric field time series is segmented into three consecutive parts, each having a length of

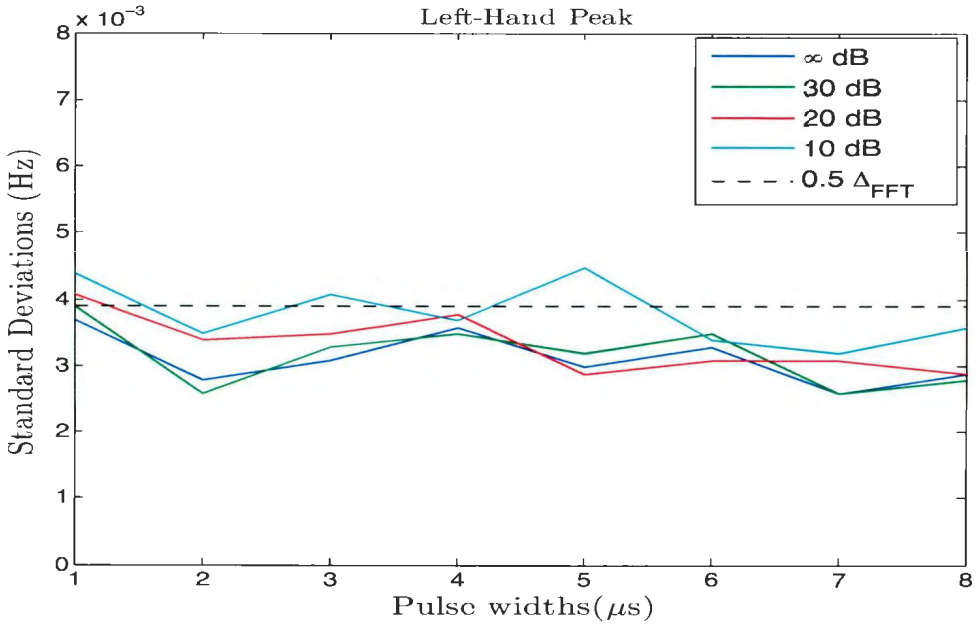

Figure 4.11: The standard deviations of the centroid positions as a function of the pulse width and SNR for the left-hand peak. The operating frequency is 25 MHz

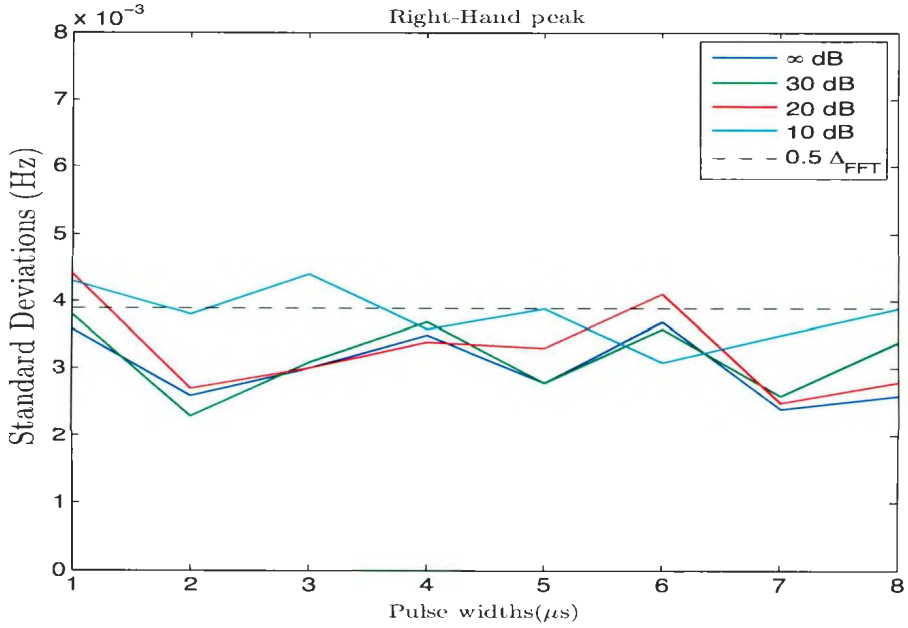

Figure 4.12: The standard deviations of the centroid positions as a function of the pulse width and SNR for the right-hand peak. The operating frequency is 25 MHz

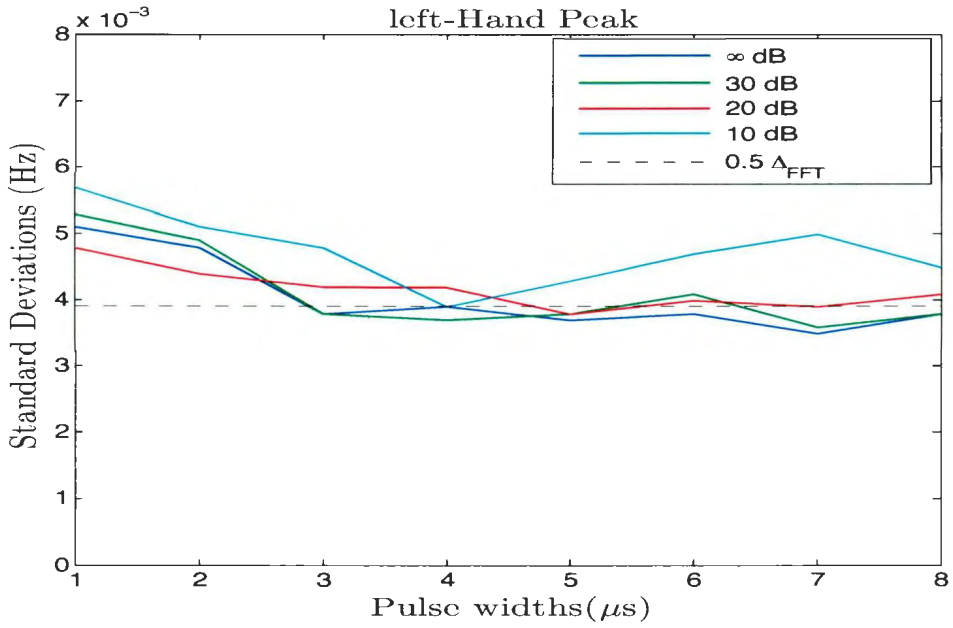

Figure 4.13: The standard deviations of the centroid positions as a function of the pulse width and SNR for the left-hand peak. The operating frequency is 15 MHz.

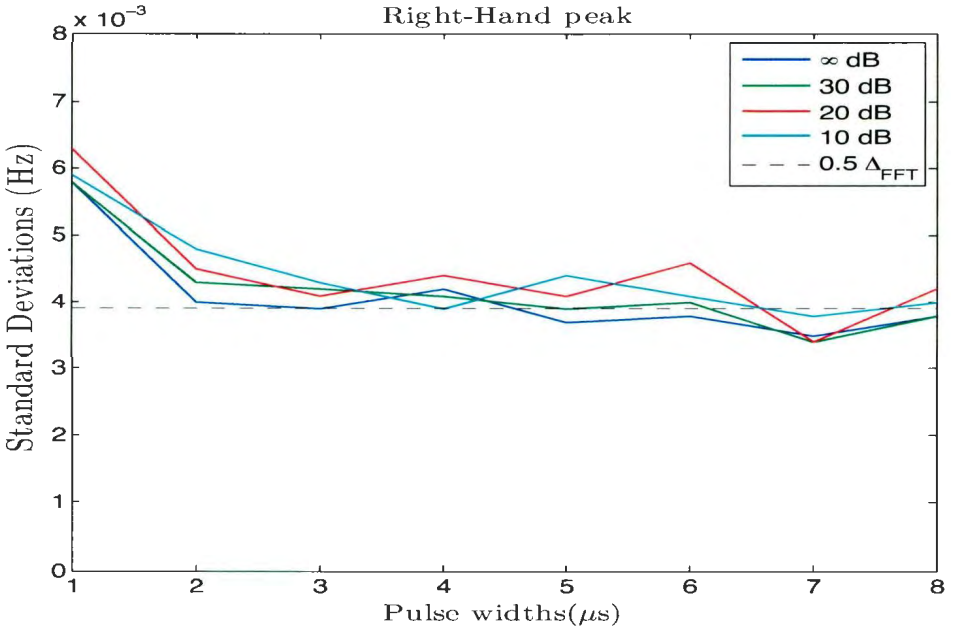

Figure 4.14: The standard deviations of the centroid positions as a function of the pulse width and SNR for the right-hand peak. The operating frequency is 15 MHz.

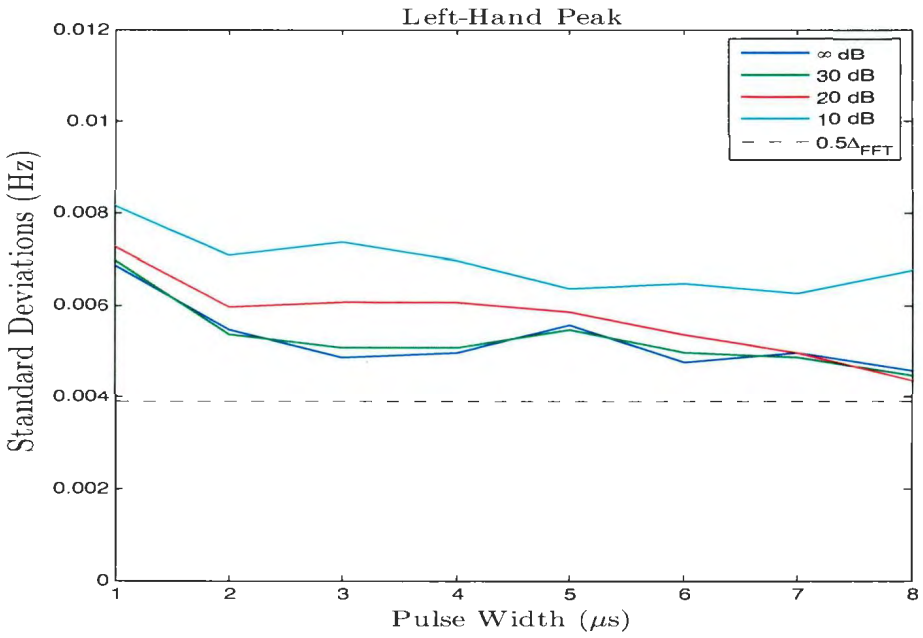

Figure 4.15: The standard deviations of the centroid positions as a function of the pulse width and SNR for the left-hand peak. The operating frequency is 5 MHz.

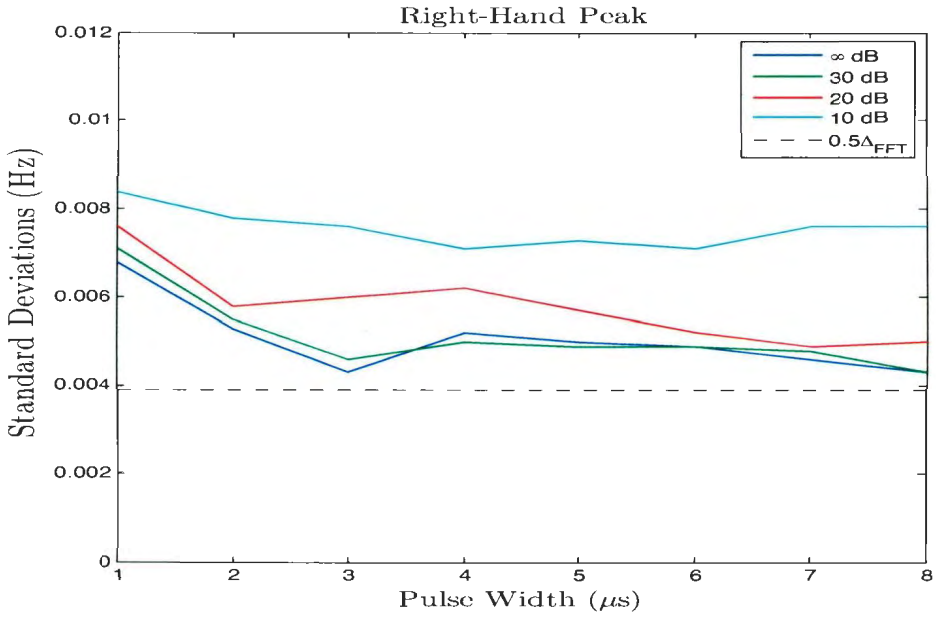

Figure 4.16: The standard deviations of the centroid positions as a function of the pulse width and SNR for the right-hand peak. The operating frequency is 5 MHz.

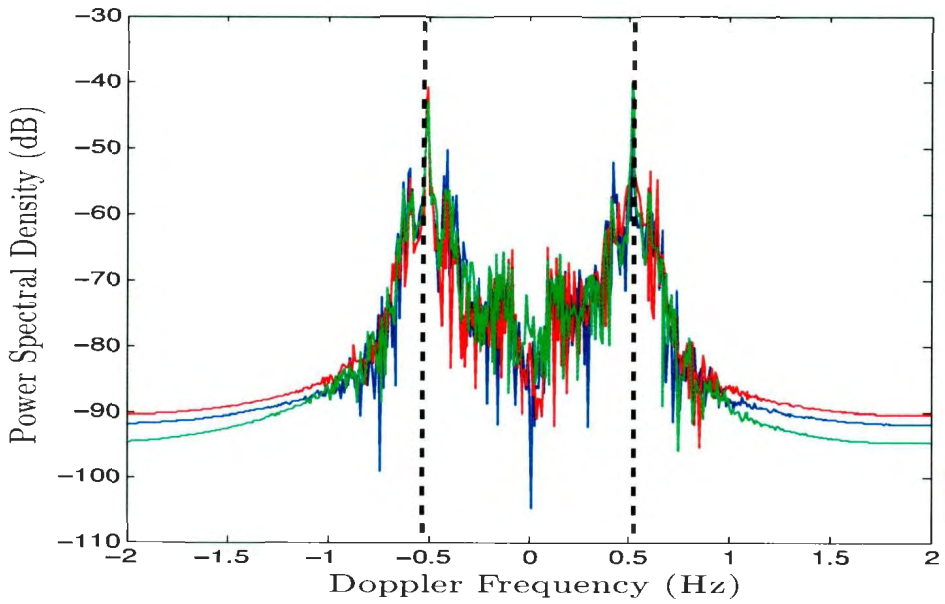

Figure 4.17: Fluctuations of the centroid postions for f_0 and $B = 100$ kHz

512 points. The PSD is estimated for each segment, and the centroid positions of the Bragg regions are located. Figure 4.17 shows the Doppler spectra for $f_0 = 25$ MHz and $B = 100$ kHz. For each segment, the centroid positions of the Bragg peaks are indicated by black dashed lines. A closer look at the Bragg regions (see Figure 4.18) shows the variations in the magnitudes of the Bragg peaks. This is one of the major causes of the fluctuations of the centroid positions.

4.4.1 Standard Deviations of the Centroid Positions

Since the pulse width of the pulsed waveform radar system is related to the bandwidth B by

$$\tau_0 = \frac{1}{B}, \tag{4.2}$$

the range of values chosen for the bandwidth for the FMCW waveform is

$$125 \text{ kHz} \leq B \leq 1000 \text{ kHz}, \tag{4.3}$$

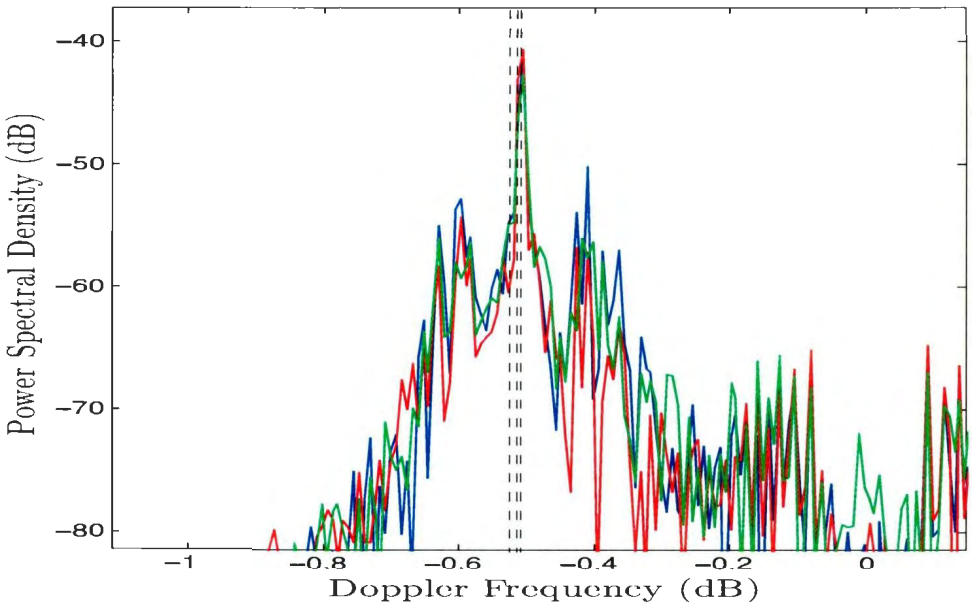

Figure 4.18: A closer look at the left-hand peak region of Figure 4.17. The centroid positions are indicated by dashed lines.

and this corresponds to

$$1 \ \mu s \leq \tau_0 \leq 8 \ \mu s \tag{4.4}$$

in the pulse waveform analysis. It may be recalled that the fluctuations are considered to be significant when the standard deviations exceed the $0.5\Delta_{\mathrm{FFT}}$. To calculate the standard deviations of the centroid positions, a long electric field time series of 65536 points corresponding to a time of 273.0667 minutes, is generated using equation (2.34). The signal is segmented into 128 consecutive part, each having a lenth of 512 points. The PSD is estimated for each segment and the centroid positions of the Bragg regions are calculated. In Figures 4.19 and 4.20, the standard deviations are plotted against the frequency bandwidth for various radar operating frequencies of 25 MHz, 15 MHz and 5 MHz. The $0.5\Delta_{\mathrm{FFT}}$ is indicated by black dashed lines. A sampling rate of 0.25 s for a 512-point FFT giving $0.5\Delta_{\mathrm{FFT}}$=0.0039, is used. It may be noticed that the standard deviation

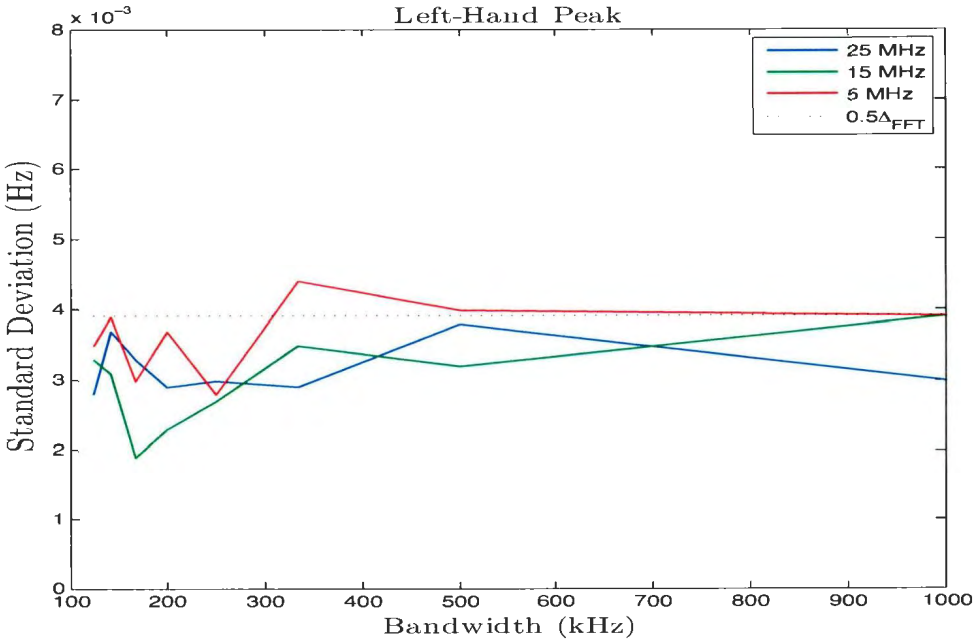

Figure 4.19: Plots of the standard deviations of the centroid positions as a function of frequency bandwidth and operating frequencies of 25 MHz, 15 MHz and 5 MHz for the left-hand peak.

of the centroid positions is a function of the radar bandwidth and the operating frequency. Depending on these operating parameters, the standard deviations may or may not exceed the $0.5\Delta_{\mathrm{FFT}}$. For example, at an operating frequency of 5 MHz and a bandwidth of 500 kHz (see Figure 4.19), the standard deviation is seen to exceed 0.0039 and thus makes the fluctuations significant. However in the same figure when the frequency is 5 MHz and the bandwidth is 250 kHz, the standard deviation is seen to be below 0.0039. This makes the fluctuations insignificant.

4.5 General Chapter Summary

A realistic way of estimating the errors associated with ocean current measurements requires an analysis that reflects what generally happens in practice. Under Pierson's model [37], the ocean surface has been described as a Gaussian random

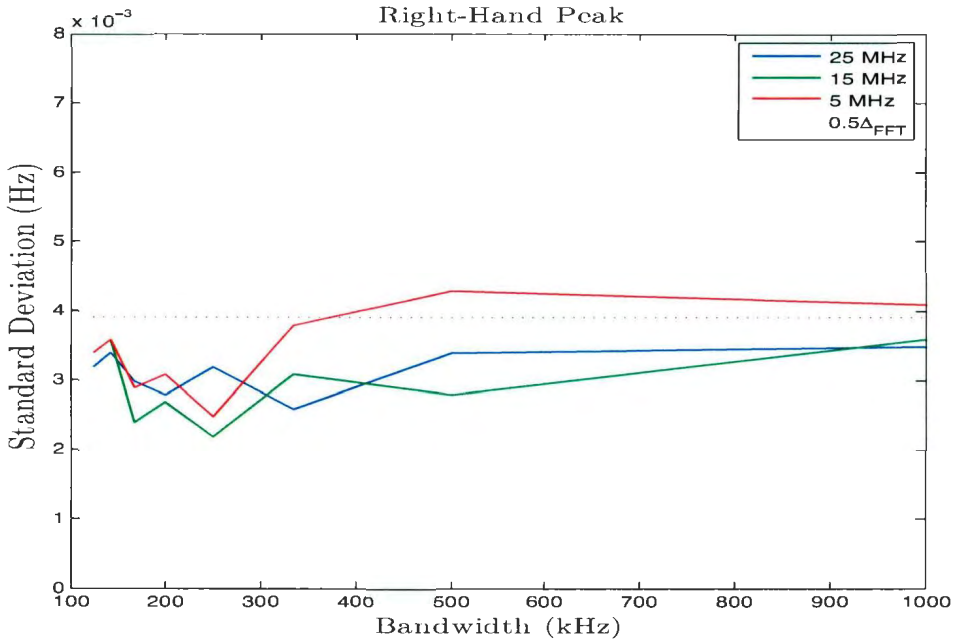

Figure 4.20: Plots of the standard deviations of the centroid positions as a function of frequency bandwidth and operating frequencies of 25 MHz, 15 MHz and 5 MHz for the right-hand peak.

process. When the ocean surface is illuminated by HF radar signals, the received signal will also be Gaussian in nature [30]. As a result of this, fluctuations occur in the Bragg peaks in the Doppler spectrum. In Zhang *et al* [8], these fluctuations were extensively examined. However, the effects of external noise was not considered in the analysis. In this chapter, the Bragg fluctuations are first examined for an ideal noiseless system for both a pulsed and an FMCW transmitting waveform. Using a suitable noise model introduced by Gill and Walsh [34] for a pulsed-type radar system, an addictive white Gaussian noise is incorporated in the time series electric field. The statistical properties of the fluctuations in the Bragg peaks, caused by both the random nature of the ocean surface and different noise levels are then investigated.

The standard deviations of the centroid positions have been checked for different operating parameters. It was seen that the fluctuation in the Bragg region is

a function of not only the operating frequency but also the pulse width (pulse waveform) or the bandwidth (FMCW waveform). It was also realized that, at lower HF frequency band, the fluctuations are more significant than that of a higher HF frequency band.

An examination of the Bragg fluctuations for different SNRs shows that for higher SNRs, the standard deviations of the centroid positions are barely affected by the noise floor. This is because the noise floor in the Doppler spectrum is, in this case, low enough to have little effect on the total spectral interval covered by the Bragg region. However, at lower SNRs, the randomness of the noise floor affects the location of the nulls between the second- and first-order peaks. This affects the the calculation of the total area covered by the Bragg region and hence the determination of the centroid positions. Therefore, minimizing the errors, generally requires a high SNR and an optimum combination of operating parameters, including the choice of frequency and pulse width or, equivalently, bandwidth.

Chapter 5

Conclusions

5.1 General Summary

The main purpose, that being the investigation of factors that affect error bounds in any parameter extracted from the HF radar received signal, has been accomplished in this study. The outcomes of this work are intended to help improve existing models used for the application of HF radar to the measurement of ocean surface currents.

5.1.1 The Problem

Pierson's model [37] describes the ocean surface as having wave components with which are associated random phases uniformly distributed over 0 to 2π. This model assumes that the ocean surface is a zero-mean Gaussian random process. As verified by Barrick and Snider [30], any linear operation on a Gaussian random variable produces another Gaussian random variable. Therefore, when HF radar signals are used to probe the ocean surface, the signal received from the ocean is Gaussian.

In calculating the Doppler spectrum of the received signal, if an infinite length

electric field time series is used as assumed in Walsh *et al* [21], and Walsh and Dawe [22] , the Doppler spectrum can be determined at each frequency component. This is because the random terms in the expression would be averaged out eventually [21]. However, in practice, measurements are always taken over finite time. Also, the HF radar system generally has an externally noise limited reception. This introduces variations in the Doppler spectrum of the received signal. In ocean surface current measurement, the location of the Bragg peaks are used for the calculation of surface current velocity. Due to the randomness in the Bragg peaks, an investigation needs to be conducted to examine the significance of these variations on ocean current measurement.

5.1.2 Solution

To address the problem, a finite electric field series is simulated based on existing electric field expressions for both pulsed and FMCW waveforms and the power spectral density of the time series is estimated as periodograms. Various operating parameters and conditions are used for the analysis. For the case of pulse radar operation, a suitable external noise model is incorporated in the electric field equations in the time domain and Doppler spectrum estimated for various radar ranges and wind directions.

The second part of the study has looked at the fluctuations in the Bragg peaks of the Doppler spectrum. The long time series is segmented into equal length consecutive sequences. The power spectral density of each segment is estimated as a periodogram. The centroid positions of the Bragg peaks are estimated and compared to theoretical values. The standard deviations of the centroid positions are calculated and compared to half the FFT resolution to check their significance. The Bragg fluctuations are assumed to be significant if the standard deviations

exceeds half the FFT resolution. The results have shown that the standard deviations of the centroid positions are dependent on the operating frequency, the sampling time, the pulse widths (pulsed waveform) and the frequency sweep bandwidth (FMCW waveform), and in some cases are significant. In particular, it was noticed that the Bragg fluctuations are more significant for lower frequency bands if other operating parameters and ocean surface conditions are fixed.

After examining the Bragg fluctuations in the Doppler spectrum caused by the random nature of the ocean only, the analysis is extended to an externally noise limited pulsed radar system. Various operating frequencies, pulse widths and signal-to-noise ratios are chosen to conduct these investigations. Based from the results obtained, the Bragg fluctuations are seen to vary for different SNRs. At higher SNRs, the standard deviations have been observed to be similar to the values obtained for an ideal noiseless system. This is because, the noise floor in the Doppler spectrum will be too low to have an influence in the calculation of the centroid positions. However, at lower SNRs, the standard deviations have been noticed to be significantly different from the that obtained for an ideal noiseless system. Thus, when the noise floor approaches the second order nulls, the calculation of the centroid positions are affected. Consequently, this affects the standard deviations in the Bragg centroids. The conclusion is drawn from this study that generally, a high SNR, approaching at least 10 dB, is required to minimize errors introduced in ocean surface current measurements.

5.2 Suggestions for Future Work

The work presented in this research provides a basis for a number of ideas in future research and experimental work.

First, although the algorithms developed in this study showed encouraging re-

sults, they still need to be checked against real data. Since an HF radar system has been installed at Placentia Bay, near Argentia, NL, Canada, the data obtained from this system could be used to validate the analysis and results presented here.

In the investigation of the Bragg fluctuations, the long time series is segmented into equal consecutive lengths of 512 point FFT. However, it would be a good idea to segment the long time series into shorter or longer consecutive lengths to examine the significance of the observation times on the Bragg fluctuations.

An obvious next step along this line of research is the analysis of the Bragg fluctuations in an externally noise limited FMCW waveform radar system after the noise is properly introduced into the FMCW electric field equations. The analysis can be carried out for various operating parameters and conditions at different noise levels.

In the investigation provided here, the effect of swell is ignored in calculating the centroid positions of the Bragg regions and the standard deviations of the centroid positions. In any future analysis, the effects of swell contamination may be considered also.

The analysis presented here can also be extended to the bistatic radar system. This study would be facilitated by the fact that models have already been developed for a pulsed radar waveforms in bistatic systems [40].

Bibliography

[1] L. Sevgi, A. Ponford, and H. C. Chan, "An integrated maritime surveillance system based on high-frequency surface-wave radars, part 1: Theoritical background and numerical simulations," *IEEE Antennas and Propagation Magazine*, vol. 43, no. 4, pp. 28–43, 2001.

[2] J. Barnum, "Ship detection with high-resolution hf skywave radar," *IEEE Journal of Oceanic Engineering*, vol. 11, no. 2, pp. 196–209, April 1986.

[3] B. Lipa, "Derivation of directional ocean wave spectra by integral inversion of the second order radar echoes," *Radio Science*, vol. 12, no. 3, pp. 425–434, 1977.

[4] D. E. Barrick, "Extraction of wave parameters from measured hf radar sea-echo doppler spectra," *Radio Science*, vol. 12, pp. 415–424, 1977.

[5] R. Howell and J. Walsh, "Measurements of the ocean wave spectra using narrow beam hf radar," *IEEE Journal Oceanic Engineering*, vol. 18, no. 3, pp. 296–305, 1993.

[6] E. W. Gill and J. Walsh, "Exraction of ocean wave parameters from hf backscatter recaived by a four element array: Analysis and application," *IEEE Journal Oceanic Engineering*, vol. 17, no. 4, pp. 376–386, 1992.

[7] D. D. Crombie, "Doppler spectrum of sea echo at 13.56 mc/s," *Nature*, vol. 175, pp. 681–682, 1955.

[8] J. Zhang, J. Walsh, and E. W. Gill, "Inherent limitations in high-frequency radar remote sensing based on bragg scattering from the ocean surface," *IEEE Journal of Oceanic Engineering*, vol. 37, no. 3, pp. 395–406, 2012.

[9] D. Pritchard, *The Radar War: Germany's Pioneering Achievement, 1904-45*. Patrick Stephens Limited, Wellingborough, England, 1989.

[10] R. Stewart and J. Joy, "Hf radio measurements of surface currents," *Deep-sea Research*, vol. 21, pp. 1039–1049, 1974.

[11] D. Barrick, J. Headrick, R. Bogle, and D. D. Crombie, "Sea backscatter at hf: interpretation and utilization of the echo," *Proceedings of the IEEE*, vol. 62, pp. 673–680, 1974.

[12] *IEEE Standard Definitions of Terms for Antennas*, Antenna Standards Committee of the IEEE Antennas and Propagation Society., 1993.

[13] D. Barrick, "First-order theory and analysis of mf/hf/vhf scatter from the sea," *IEEE Transactions on Antennas and Propagation*, vol. 20, pp. 2–10, 1972.

[14] S. Rice, "Reflection of electromagnetic waves from a slightly rough surface," *Theory of Electromagnetic Waves*, pp. 351–378, 1951.

[15] D. Barrick, "Remote sensing of sea state by radar," in *Remote Sensing of the Tropo-sphere*, v. derr, ch. 12, pp. 1–46 ed. DC: U.S. Government Printing Office, 1972.

[16] D. Barrick and B. Lipa, "The second-order shallow water hydrodynamic coupling coefficient in interpretation of hf radar sea echo," *IEEE Journal Oceanic Engineering*, vol. 11, no. 2, pp. 310–315, 1986.

[17] B. Lipa and D. Barrick, "Analysis methods for narrow-beam high-frequency radar sea echo," *Technical Report ERL 420-WPL 56, National Oceanic and Atmospheric Administration*, 1982.

[18] B. J. Lipa and D. E. Barrick, "Extraction of sea state from hf radar sea echo: Mathematical theory and modeling," *Radio Science*, vol. 21, pp. 81–100, 1986.

[19] L. Wyatt, "The measurement of the ocean wave directional spectrum from hf radar doppler spectra," *Radio Science*, vol. 21, no. 3, pp. 478–485, 1986.

[20] S. Srivastava, "Analysis of hf scattering from an ocean surface: An alternative approach incorporating a dipole source," PhD thesis, Memorial University of Newfoundland, St. John's, Newfoundland, 1984.

[21] J. Walsh, R. Howell, and B. Dawe, "Model development for evaluation studies of ground wave radar," Contract Report 90-C14, Centre for Cold Ocean Resources Engineering, (Prepared for Department of National Defence, Government of Canada, DSS Contract Number W7714-8-5655/01-SS), 1990.

[22] J. Walsh and B. Dawe, "Development of a model for the first-order bistatic ocean clutter radar cross section for ground wave radars," contract report, Northern Radar Systems Limited, (Prepared for the Defence Research Establishment Ottawa, Department of National Defence, Government of Canada, DSS Contract Number W7714-1-9565/01-ST), 1994.

[23] E. W. Gill and J. Walsh, "High-frequency bistatic cross sections of the ocean surface," *Radio Science*, no. 6, pp. 1459–1475, 2001.

[24] E. Gill and J. Walsh, "High-frequency bistatic cross sections of the ocean surface," *Radio Science*, vol. 36, no. 6, pp. 1459–1475, 2001.

[25] P. Bobby, "Estimation of vector current beyond the region of overlap of dual-site hf radar: An implementation of the continuity equation," Master's thesis, Memorial University of Newfoundland, St. John's , Newfoundland, 2003.

[26] Q. Jin, "An algorithm for the extraction of ocean surface current velocity from bistatic hf groundwave radar data-a simulation," Master's thesis, Memorial University of Newfoundland, St. John's , Newfoundland, 2007.

[27] J. Zhang and E. W. Gill, "Extraction of ocean wave spectra from simulated noisy bistatic high–frequency radar data," *IEEE Journal of Oceanic Engineering*, vol. 31, no. 4, 2006.

[28] D. Green and E. W. Gill, "Extracting wind parameters from high frequency ground wave radar backscatter," IEEE AP-S International Symposium and USNC/ URSI National *Radio Science Meeting* (Washing, DC, USA), Tech. Rep., 2005.

[29] W. Huang, E. Gill, X. Wu, and L. Li, "Measurements of sea surface wind direction using bistatic high-frequency radar," *IEEE Trans. Geoscience Remote Sensing*, vol. 50, no. 10, pp. 4117–4122, 2012.

[30] D. Barrick and J. Snider, "The statistics of hf sea-echo doppler spectra," *IEEE Transactions on Antennas and Propagation*, vol. 25, pp. 19–28, 1977.

[31] D. Barrick, "Accuracy of parameter extraction from sample-averaged sea-echo doppler spectra," *IEEE Transactions on Antennas and Propagation*, vol. AP-28, no. 1, pp. 1–11, 1980.

[32] T. M. Georges and R. Jones, "A mathematical model for how ionspheric reflection degrades sea echo spectra," *NOAA Technical Memorandum ERL WPL-60*, 1981.

[33] T. M. Georges and J. W. Maresca, "The effect of space and time resolution on the quality of sea echo doppler spectra measured with hf skywave radar," *Radio Science*, vol. 14, pp. 455 469, 1979.

[34] E. W. Gill and J. Walsh, "A combined sea clutter and noise model appropriate to the operation of high-frequency pulsed doppler radar in regions constrained by external noise," *Radio Science*, vol. 43, 2008.

[35] E. Gill and J. Walsh, "A relationship between external noise and the ocean clutter models for bistatic operation of a pulsed high-frequency radar," *in Proc. IEEE Canadian Conf. Electr. Comput. Eng.*, vol. 1, pp. 153–158, 2001.

[36] J. Walsh, J. Zhang, and E. Gill, "High frequency radar cross section of the ocean surface for an fmcw waveform," *IEEE Journal Ocean. Engineering*, vol. 36, no. 4, pp. 615–626, 2011.

[37] W. Pierson, "Wind generated gravity waves," *Advances in Geophysics*, vol. 2, pp. 93 178, 1955.

[38] J. Walsh and E. Gill, "An analysis of the scattering of high-frequency electromagnetic radiation from rough surfaces with application to pulse radar operating in backscatter mode," *Radio Science*, vol. 35, no. 6, pp. 1337–1359, 2000.

[39] J. R., "Electromagnetic surface waves," in *Advances in Radio Research*, E. J. A. Saxton, Ed. New York: Academic, 1964, pp. 157–217.

[40] E. W. Gill, "The scattering of high frequency electromagnetic radiation from the ocean surface: An analysis based on a bistatic ground wave radar configuration," PhD thesis, Memorial University, St. John's, Newfoundland, 1999.

[41] B. Kinsman, *Wind Waves*. New York: Dover Publications Inc., 1984.

[42] M. Tucker, *Waves in Ocean Engineering.* New York: Ellis Horwood, 1991.

[43] W. Pierson and L. Moskowitz, "A proposed spectral form for fully developed seas based upon the similarity theory of s.a. kitaigorodskii," *J. Geophys. Res.*, vol. 69, pp. 5181–5190, 1964.

[44] J. G. Proakis, *Algorithms for Statistical Signal Processing.* New Jersey: Prentice-Hall, 2002.

[45] B. Dawe, "Radio wave propagation over the earth: Field calculations and an implementation of the roughness effect," Master's thesis, Memorial University of Newfoundland, St. John's Newfoundland, 1984.

[46] P. E. Dexter and S. Theodorides, "Surface wind speed extraction from hf sky-wave radar doppler spectra," *Radio Science*, vol. 17, no. 3, pp. 643–652, 1982.

[47] W. Huang, S. Wu, B. Wen, and J. Hou, "Hf radar wind and wave measurement over the eastern china sea," *IEEE Trans. Geoscience Remote Sensing*, vol. 40, no. 9, pp. 1950–1955, 2002.

[48] *Propagation in Ionized Media(ITU-R Recommendations,1994 PI Series Volume)*, International Telecommunications Union,Geneva, 1994.

[49] A. Papoulis, *The Fourier Integral and its Application.* New York: McGraw-Hill, 1962.